EXPERIMENTAL EVALUATIONS OF ESF METHODS

EXPERIMENTAL EVALUATIONS OF ESF METHODS FOR

NEUTRON RADIOGRAPHIC IMAGE ANALYSIS   Part 8

by

MICHAEL PAUL BUTLER, B.Eng.

A Report
Submitted to the School of Graduate
Studies in Partial Fulfillment of the
Requirements for the Degree

Master of Engineering

McMaster University

1980

MASTER OF ENGINEERING (1980) McMASTER UNIVERSITY

Engineering Physics Hamilton, Ontario

TITLE: Experimental Evaluations of ESF Methods for
Neutron Radiographic Image Analysis

AUTHOR: Michael Paul Butler, B.Eng. (McMaster)

SUPERVISORS: A.A. Harms (on-campus)
P.C. Ernst (off-campus)

NUMBER OF PAGES: vi, 61

ABSTRACT

Some experiments designed to test the validity of the edge-spread function (ESF) model for neutron radiographic image formation are described; in addition the experiments are meant to illustrate the application of ESF methods to two areas of practical concern. First, the prediction of optical density curves for specified material and geometric configurations is considered; then, the use of ESF methods in dimensioning irradiated reactor fuel elements is examined. Overall, the results indicate that within the framework of assumptions which ESF theory is based upon, the correlation between theory and experiment is excellent. The results also suggest that in situations which deviate from the theoretical ideal, the ESF method may serve as a good first approximation to more complex models.

ACKNOWLEDGEMENTS

It would be rather uncouth to end this project without acknowledging the assistance of a number of individuals, all of whom helped in numerous ways. I note, however, that they let me do all the heavy lifting.

The assistance of my supervisors, Mr. Peter Ernst and Dr. Archie Harms, is appreciated; their technical expertise helped to restrain the wilder flights of radiographic fantasy.

As always, my typists did a splended job; special thanks to Miss Janet Delsey and Mrs. Kathy Noon.

The help of the operating crews of the McMaster Nuclear Reactor was greatly appreciated; all of them spared no effort in helping to clean up numerous neutron spills.

Finally, I would like to thank the thousands of young ladies who went to McMaster during my tenure; as I sat in the sun in front of the Burke Sciences Building, the sight of the endless parade of fluff helped to assuage the guilt feelings arising from knowing that I was supposed to be working.

TABLE OF CONTENTS

LIST OF ILLUSTRATIONS

1. INTRODUCTION

1.1 <u>Overview</u>

In a number of earlier works[1-4], a theoretical method for the analysis of neutron radiographic images has been developed in considerable generality. This method is called edge-spread function (ESF) analysis, and it attempts to describe the processes occurring in neutron radiography which lead to image "unsharpness", or blurring. As mentioned, the mathematics have been highly developed; unfortunately, experimental testing of this model has been limited to very simple or basic situations.[2,3]

It is the purpose of this report, then, to partially remedy this situation; some of the more practical applications of ESF theory will be examined from an experimental viewpoint, so as to properly determine whether or not the theory is of any utility. Since this is meant to be a preliminary investigation, the emphasis will tend to be on the comparison of theoretical and experimental results, rather than on the development of any sophisticated techniques. It will be shown however, that there appears to be considerable justification for the application of ESF methods; thus, in the concluding chapter there will be some discussion of the extension of these methods to commercial non-destructive testing, with some emphasis on making the techniques amenable to routine application.

This work is devoted to an experimental evaluation of the mathematical theory of neutron radiographic imaging based on the use of edge-spread functions. For ease of reference, a brief discussion of some basic principles is provided in the remainder of this chapter. The necessary mathematics and some examples of convertor response function for specific cases are presented in chapter 2.

Chapter 3 examines some simple applications of the theory, and chapter 4
considers a practical problem; specifically, the matter of dimensioning irrad-
iated reactor fuel elements will be the subject of an ESF analysis. Finally,
in chapter 5 some conclusions and suggestions for further development will
be presented.

1.2 Image Formation Processes

Before any experimental examination of ESF methods is undertaken,
a brief discussion of some of the physical processes involved is necessary;
also, an heuristic approach may aid in clarifying the mathematics which will
be developed in chapter 2. Consider figure 1-1, which shows a simple representation
of the image formation process: a collimated beam of nearly mono-energetic
neutrons strikes a sample, and its intensity is modulated according to thickness
and cross-section factors. Then, the now-heterogeneous beam passes through
the film into a convertor foil, whereupon secondary photo-effective radiation
is emitted and thus causes exposure of the film.

Several assumptions are made in the representation used here: first,
the incident beam is assumed to be perfectly collimated. While the inclusion
of beam divergence is not particularly difficult, it will be neglected for simp-
licity. This will have negligible consequences for the experimental portion
of this work, since the radiography facility used has an excellent collimation
ratio. Second, only absorption by the samples will be considered, leading to
a considerable simplification of the mathematics. The third assumption is that
beam interaction with the film is negligible; this is justified by noting that
if the neutrons were at all efficient in interacting with the film, then the
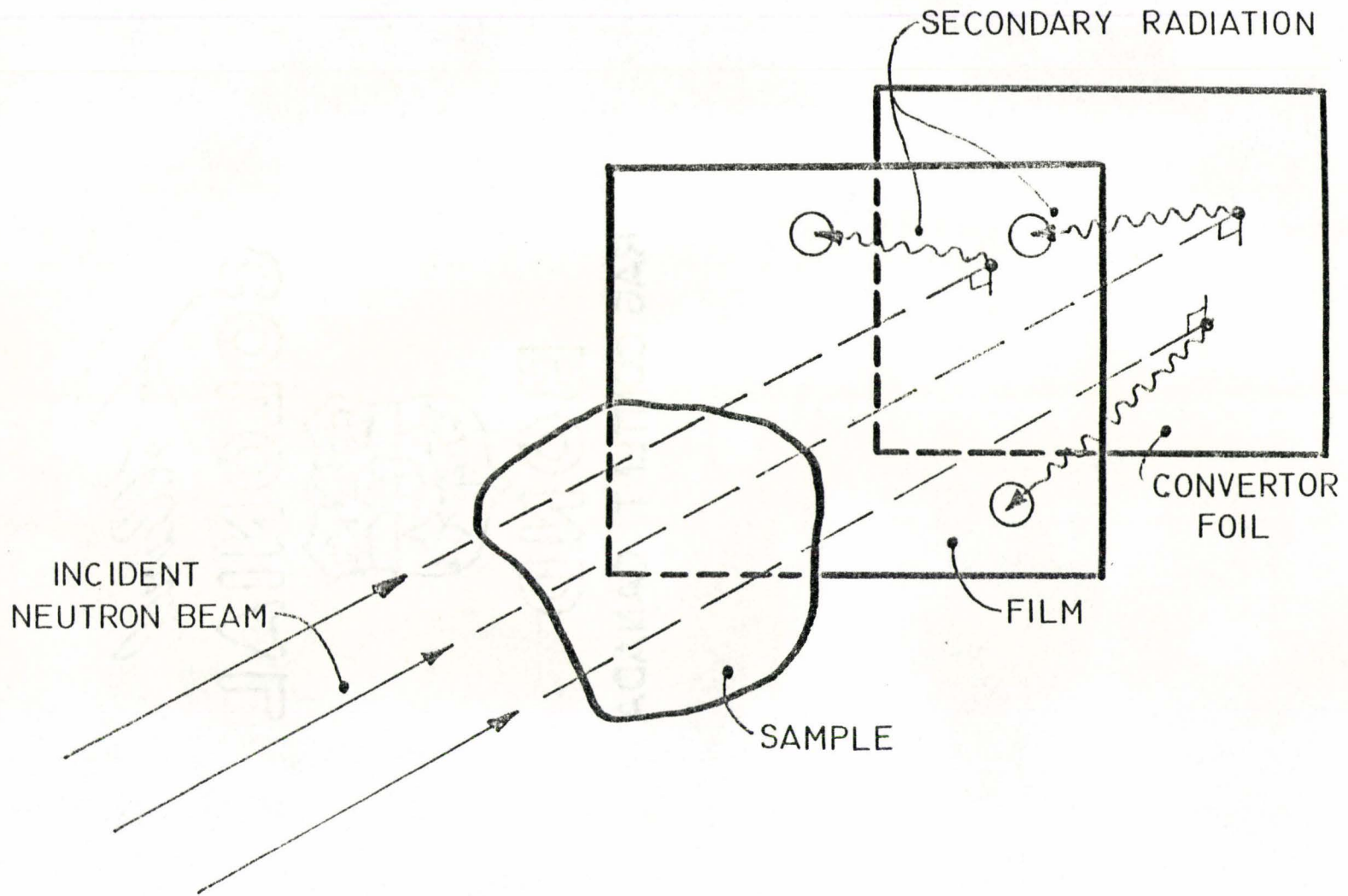
Fig. 1-1: The image formation process in neutron radiography.

3

convertor screen would not be required. Finally, the film-convertor separation is taken to be zero; note that in figure 1-1 this distance is greatly exaggerated.

The net result of these assumptions is to imply that all image "smearing" effects are due only to the conversion process, i.e. the isotropic emergence of the secondary radiation about the point of neutron absorption. This phenomenon can best be described by noting that a micro-densitometer scan of the optical density pattern resulting from a knife-edged object is not a step-function; rather, it has a "spread-out" appearance similar to that illustrated in figure 1-2. The end result of the secondary radiation source divergence is to create uncertainty in a number of types of measurement; for example, obtaining the dimensions of an object from a radiograph becomes increasingly difficult as higher orders of accuracy are required, since the spreading effect becomes increasingly significant.

The main point to be made is that a means of predicting the convertor response (and thus the optical density) is required which accounts for the spreading phenomena, and in addition takes into consideration other object parameters, such as shape and cross-section. The approach to be used in this work utilizes the edge-spread function method; the mathematical framework needed is the subject of chapter 2.

1.3 Relationship between Convertor Response and Optical Density

As described in the previous section, the quantity obtained in the preliminary calculations is the convertor response, or fractional screen flux. However, this is not the quantity which is measured from
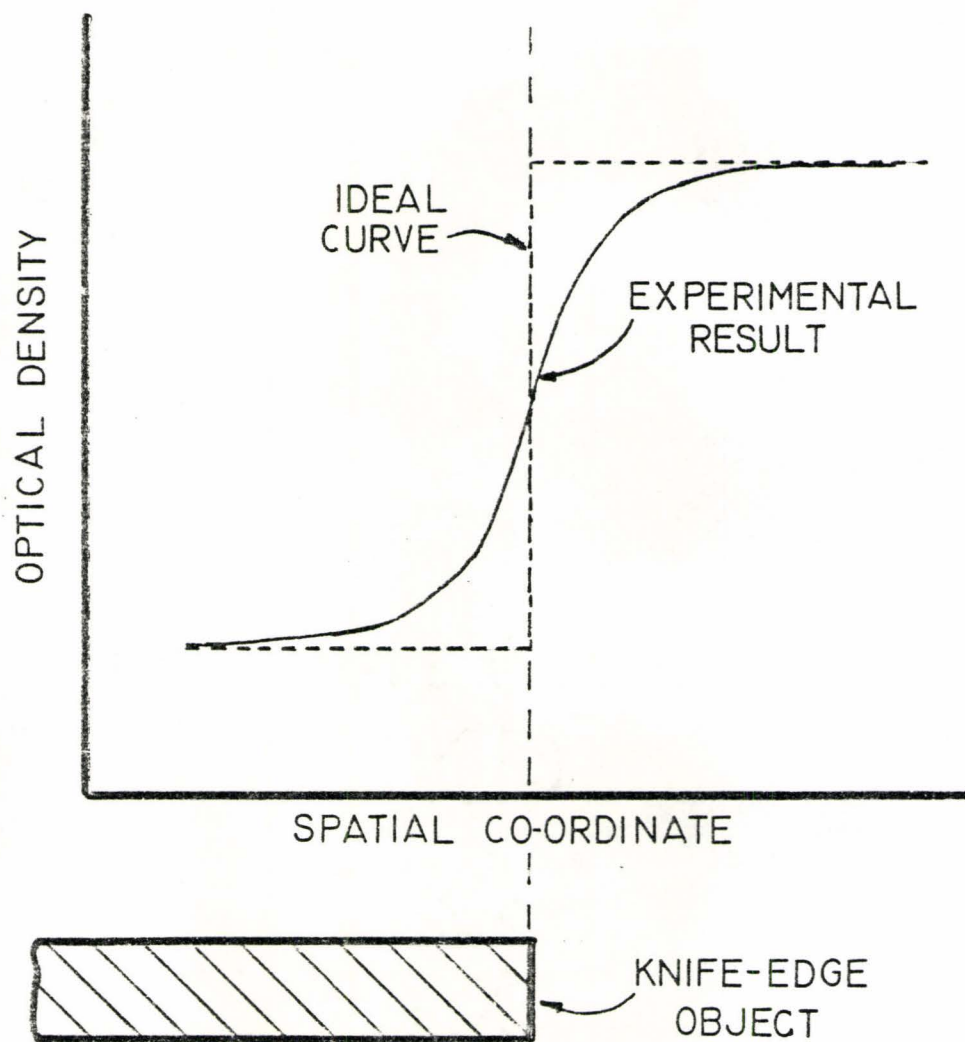
Fig. 1-2:   Ideal and actual optical density curves for a knife-edge object.

a radiographic image; rather, the optical density, or the film blackness is being examined. This quantity is defined in terms of the incident and transmitted light fluxes thus:

$$D = \text{Optical Density} \equiv \log_{10}[I_0/I_T] \qquad (1.1)$$

The logarithmic definition is of no particular importance; it merely serves to reduce the range of the independent variable, since the density is a rather slowly-varying function of the exposure for the case of neutron radiography.

One point of importance here is the matter of background density, or film "fog"; this is the inherent optical density of the film, and is due to the material of the film base and to the film development processes. It is possible to ignore the background density in any analysis; however, it is usually subtracted from all measurements, according to standard procedures, since this allows a more direct correlation between density and exposure, i.e. zero exposure giving zero density. This procedure will be adopted throughout this report, so that all values quoted for optical density will be such that

$$D_{actual} = D_{measured} - D_{back} \qquad (1.2)$$

where D_{back} is the value appropriate to the type of film being discussed.

Now, some relationship is required which gives optical density as a function of convertor response; very generally, a transformation T is required such that

$$D(x) = T\{S_A(x)\} \tag{1.3}$$

where $S_A(x)$ is the convertor response, or "secondary flux".

The two most likely forms for T are graphical and polynomial transforms; the former requires knowledge of density-exposure relationships, as given by manufacturer specification sheets, while the latter only involves curve-fitting: one specifies $D(x)$ such that

$$D(x) = \sum_{i=1}^{N} C_i[S_A(x)]^i \tag{1.4}$$

where N is very likely to have a maximum value of 2 or 3. It has been suggested that a linear fit will be sufficient, but it appears to this author, on the basis of preliminary work,[2] that a quadratic form is more appropriate: the linear fit seems best suited to higher values of optical density, which may not be routinely achieved in practice. Nonetheless, in this work a linear model will generally be used so as to simplify the calculations.

Admittedly, more sophisticated models are available; for example, the following has been used to good effect in some instances:[5]

$$\frac{D}{D_{max}} = 1 - e^{-an} \sum_{j=1}^{r} \frac{(an)^{j-1}}{(j-1)!} \tag{1.5}$$

where a = film grain area,

   n = number of incident photons per unit area,

   r = number of "hits" required to make the emulsion grain developable.

However, this model requires a knowledge of both the film-grain character-
istics and the statistical properties of the incident photo-flux: one has
to be able to specify an appropriate value for n. In general, the amount of
difficulty required to implement the more sophisticated models is not worth
the very slight gains in accuracy; thus, for the purposes of this work, the
simple convertor response/density transform will be used for the sake of
simplicity and compactness. In addition, emphasis will be placed on the
polynomial techniques, since these lend themselves to greater numerical
accuracy, and are ideal for use on a computer.

1.4 Experimental Facilities

This section deals with the equipment used to obtain the experimental
data examined in this report. To some extent, a "black box" approach will
be used, in that specific details of a given instrument will not be considered.
This is of small consequence, since the purpose of this report is to consider
data obtained from existing equipment, rather than to make any major modifica-
tions to the present set-up.

The basic apparatus consists of the Vertical Through-Tube illustrated
in figure 1-3. Neutrons in the core are moderated and scattered by approxi-
mately one foot of graphite in the bottom of the tube, which has been
placed in an empty position in the grid plate that makes up the base of the
core. This neutron beam is then collimated to a diameter of one inch by
about eleven feet of lead shot and small polyethylene beads contained
between two aluminum annuli. Over the remaining length of aluminum tube,
the beam spreads out to a diameter of approximately two and three-quarter
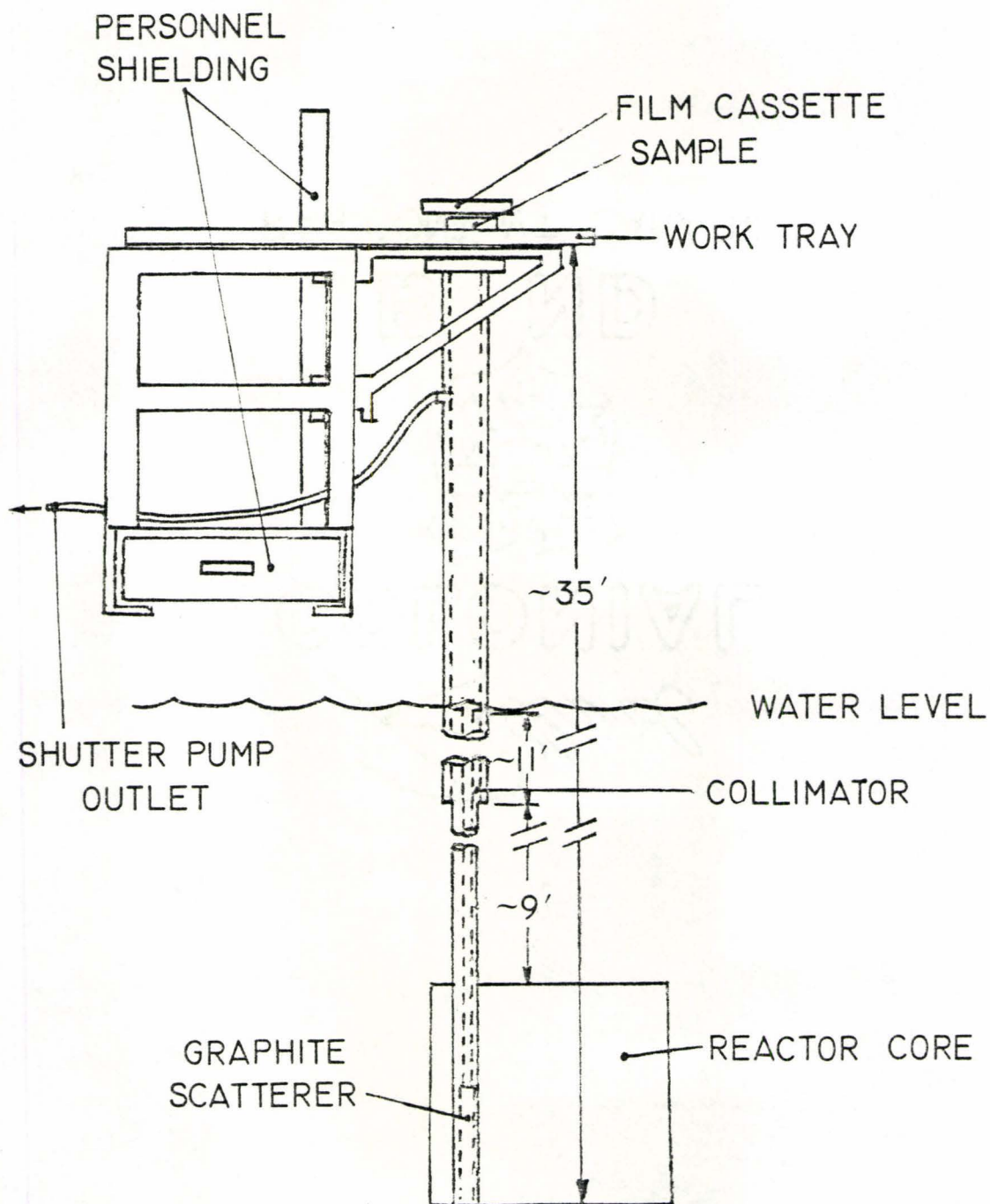inches. Taking the divergence length as the distance from the top of the

Fig. 1-3: The vertical through-tube facility for neutron radiography experiments at the McMaster Nuclear Reactor. The water shutter is not shown.

collimator to the end of the tube, or fifteen feet, then the angle of
beam divergence, θ_d, is

$$\theta_d \simeq \tan^{-1} \left(\frac{0.875}{12 \times 15} \right)$$

$$= 0.28°$$

In other words, the beam diameter increases by about five millimetres for
every metre one moves away from the collimator. This collimation ratio
is quite acceptable for purposes of neutron radiography.

Above the collimator is a water shutter; this is simply a large
aluminum canister which is drained or filled by means of a small electric
pump. When the shutter is pumped full, the depth of water is sufficient
to cut off about ninety-five percent of the beam intensity.

At the top of the through tube, there is an aluminum work tray
for holding samples and film cassettes. The tray metal is one-eight of
an inch thick; the resulting attenuation of the beam is about 0.5 percent,
so that any effects the tray may have on the neutron beam can be neglected
in the analysis.

The remaining components of this radiography facility consist of
the personnel shielding (two boxes filled with wax), the inlet/outlet line
for the water, a small pump, and an auxiliary storage tank for the water
pumped out of the tube. All parts are removable.

In considering the radiation beam created with this facility, one
must note that the beam is not "pure"; in other words, there are radiations

other than thermal neutrons present. Using an ASTM beam purity indicator[6],
it has been found that the make-up of the beam is as shown in Table 1-1.
As will become apparent, the relatively large γ-ray content may lead to
some difficulty in interpreting any results (cf. chapters 3 and 4).

The actual flux of thermal neutrons can be very roughly estimated
in the following manner: for optical densities around unity (the film
blackness through which the letters on a printed page can just be made out),
an often quoted[7] figure for the minimum necessary time-integrated flux
is 10^9 n/cm^2. Using this facility, unit optical density can be obtained
in about seven to fifteen minutes, depending on film type and reactor power
level. Clearly, the flux can be determined from

$$\phi' = \phi/T_e \tag{1.6}$$

where ϕ is the integrated flux (n/cm^2), ϕ' is the "flux rate" (n/cm^2-sec),
and T_e is the exposure time. Using the numbers given previously, the result-
ing estimated flux is such that

$$1.1 \times 10^6 \leq \phi' \leq 2.4 \times 10^6 \text{ n/cm}^2\text{-sec}$$

This result should be viewed with some caution, since it assumes that the
film blackening is entirely due (indirectly) to thermal neutrons, whereas
in reality the γ-radiation also tends to blacken the film. If one assumes
that the optical density specifically caused by a given type of radiation
is proportional to the amount of that radiation in the beam, then the values
given in Table 1-1 can be used to correct the flux values given previously:

$$\phi'' = 0.7\phi' \tag{1.7}$$

Table 1-1: Radiation Content of the VTT Beam

Type of Radiation	Approximate Content (%)
Thermal neutrons	65
Low-energy γ's	25
Epithermal neutrons	5
Scattered neutrons	5

N.B. 1) Values are obtained using an ASTM beam purity indicator.

2) Scattered neutrons are assumed to be thermal, so that the total thermal content is $\approx 70\%$.

where ϕ'' is the flux corrected to represent neutron exposure only. This changes the estimated range of flux values to

$$7.7 \times 10^5 \leq \phi'' \leq 1.7 \times 10^6 \quad \text{n/cm}^2\text{-sec}$$

Again, it should be noted that this result is only approximate.

The films used for this work were Kodak Types AA and T industrial radiography films. Type AA is medium-grain, high speed film, and was used for set-up work because relatively short exposure times were required to obtain sufficient optical density for the purpose of analysis. Type T is fine-grained, slow film; it appears that about one and one-half to two times the exposure required for Type AA is necessary to achieve the same blackness on Type T, but the fine grain helps to cut down experimental "noise". Both film types were developed using standard procedures, which is to say five minutes in the developer, one minute in the stop bath, about three minutes in the fixer, and then prolonged washing in water. A small darkroom was set up in the reactor building to facilitate film handling.

To analyze the radiographs, a number of densitometers were used. In particular, two spot densitometers were used for in-place measurements of absolute density, and a Leitz scanning micro-densitometer with a Hewlitt-Packard chart recorder was used for relative measurements over greater distances. Some of the difficulties involved in applying these devices are discussed in chapters 3 and 4.

Finally, to analyze the numerical data obtained from the radiographs, a program was written which was capable of predicting the convertor response for any combination of materials and geometry; if desired, the program is also capable of comparing these theoretical results to experimental data. To this

end, extensive use was made of McMaster's CDC6400 and CYBER 170/30 compu-

ters.

2. MATHEMATICAL PRELIMINARIES

2.1 The Theory of Edge-Spread Function Methods

In the previous chapter, a brief description of the processes leading to neutron radiographic image formation was given, in terms of the physical concepts involved. The purpose of the present chapter is to outline the theory behind a particular model which has been developed to describe these processes in mathematical terms. The model to be described is the so-called edge-spread function method, which has been used to some extent as an alternative to the more complicated optical transfer function methods; these make considerable use of Fourier transform techniques. The ESF method has been developed to a considerable extent in recent years, at least with regard to its applications to neutron radiography; the initial basic applications of the theory can be found in references 1 and 3, while the generalized theory can be found in references 2 and 4. Since the theoretical background is well-established, only an outline of the mathematics will be given here.

In modelling the image formation process, one needs to consider both the effects of sample properties and the effects of the convertor foil on the neutron beam. The former causes the beam intensity to become non-uniform; since only sample absorption is being considered here (cf. section 1.2), then this non-uniformity can be described by an exponential expression which might be called the attenuation function:

$$\phi(u) = \exp\left\{ -\int_{z_n(u)}^{z_p(u)} \Sigma_a(u,z)dz \right\} \tag{2.1}$$

Here, z_p and z_n are the upper and lower limits of the object thickness at the point $x = u$; the geometry is illustrated in figure 2-1. $\Sigma_a(u,z)$ is the macroscopic absorption cross-section.

To examine the effects of the convertor foil, one can view the conversion process as being governed by a probability distribution. In other words, the probability of secondary radiation striking the film in a region du about a point x, after emission from the convertor at point u, is given by

$$NL(x,u)du \qquad (2.2)$$

$L(x,u)$ is called a line-spread function (LSF); N is a normalization constant, yet to be specified. If one now takes the product of equations (2.1) and (2.2), the resulting function is indicative of the fraction of the total secondary radiation emitted by the convertor which ends up in the region du after the neutron beam is attenuated by the sample. This is called the fractional convertor response, and is denoted by

$$dS_A = NL(x,u)\phi(u)du \qquad (2.3)$$

The subscript "A" refers to sample absorption. Clearly, the total convertor response is given by

$$S_A(x) = N \int_{u=-\infty}^{+\infty} L(x,u)\phi(u)du \qquad (2.4)$$

To determine a value for N, one takes advantage of the fact that $L(x,u)$ is a probability distribution, and thus must satisfy the condition
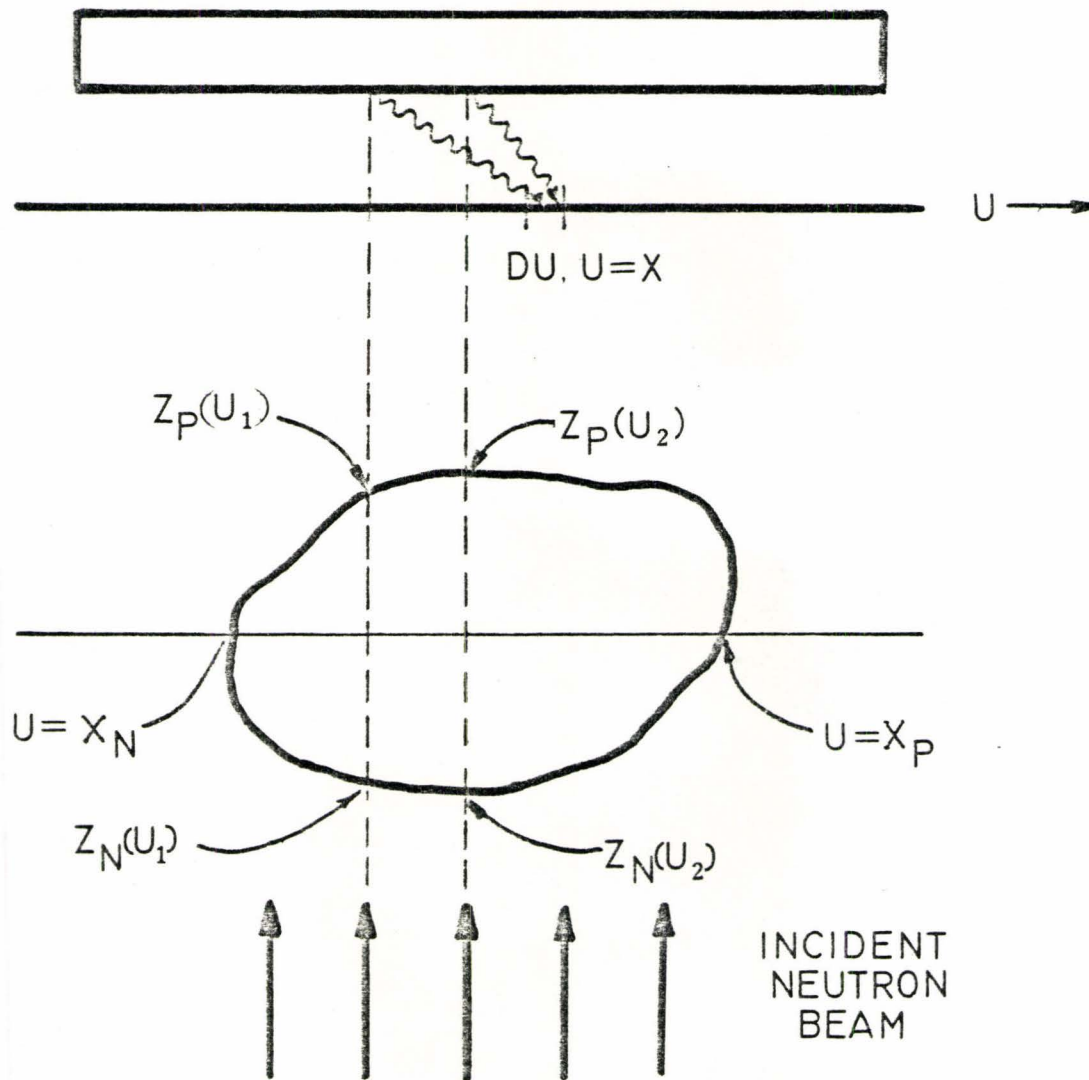
Fig. 2-1: Symbolism used in developing the mathematics for an ESF analysis.

$$N \int_{u=-\infty}^{+\infty} L(x,u)du = 1 \tag{2.5}$$

This requires specifying a form for $L(x,u)$, which is not overly difficult; it has been found[3] that a suitable expression for the purposes of neutron radiography is the Lorentzian defined by

$$L(x,u) = \frac{1}{1 + C(x-u)^2} \tag{2.6}$$

C is the so-called Lorentzian coefficient, and has units of inverse length-squared. If this is substituted into equation (2 5), then one can show that

$$N = \sqrt{C}/\pi \tag{2.7}$$

Thus, the final form for the convertor response is

$$S_A(x) = \frac{\sqrt{C}}{\pi} \int_{u=-\infty}^{+\infty} L(x,u)\phi(u)du \tag{2.8}$$

This expression can be put into a more useful form by noting that beyond the object boundaries there is no material attenuation of the neutron beam; then, since $\Sigma_a(u,z)$ is zero, $\phi(u)$ is equal to unity, and as a result the equation for the convertor response becomes

$$S_A(x) = 1. + \frac{1}{\pi} \{\tan^{-1}[\sqrt{C}(x-x_p)] - \tan^{-1}[\sqrt{C}(x-x_n)]\}$$

$$+ \frac{\sqrt{C}}{\pi} \int_{x_n}^{x_p} L(x,u)\phi(u)du \tag{2.9}$$

Here, x_n and x_p are the left- and right-hand boundaries of the object, corresponding to its edges.

There are a number of ways in which equation (2.9) can be applied. For example, if the dimensions, material properties, and geometry of a sample are known, then the convertor-response (and eventually the optical density) corresponding to that object can be predicted. Contrarily, if the dimensions are not known, then some sort of iterative method, or perhaps a least squares technique, could be used to determine values for these dimensions. These two ideas are examined in chapters 3 and 4 respectively and, as will become apparent, the results indicate that with some refinement, ESF methods may be very useful in non-destructive examinations. However, before proceeding on to the experimental work, the convertor response functions for the samples to be considered will be derived; this will be the subject of the next section.

2.2 Specific Examples of Convertor Response Functions

Since the derivation of the convertor response function is a fairly straight-forward matter for any object of known properties, it seems that it would be convenient to collect all the functions together in tabular form, along with a figure illustrating the relevant features of each object. To further simplify matters, note that regardless of the nature of $\phi(u)$, the expression for $S_A(x)$ (cf. equation 2.9) always contains the terms

$$S_o(x) \equiv 1. + \frac{1}{\pi} \{\tan^{-1}[\sqrt{C}(x-x_p)] - \tan^{-1}[\sqrt{C}(x-x_n)]\} \qquad (2.10)$$

The only differences in the form of $S_A(x)$ arise because of the integral term; thus, let a "perturbation" function be defined by

$$P(x) = \frac{\sqrt{C}}{\pi} \int_{u=x_n}^{x_p} L(x,u)\phi(u)du \qquad (2.11)$$

This function is shown in Table 2-1, along with the figures. It is clear that the convertor response function is now given by

$$S_A(x) = S_o(x) + P(x) \qquad (2.12)$$

In the interest of simple notation, some definitions will be made here which will be used througout the remainder of this work. Because the inverse tangent function appears so often, it will be denoted by the following short forms:

$$t(u) \equiv \tan^{-1}[\sqrt{C}(x-u)]$$
$$t(u)\Big|_W \equiv \tan^{-1}[\sqrt{C}(w-u)] \qquad (2.13)$$

Using this notation and equation (2.6), the integral of the Lorentzian function can be easily shown to be

$$\int_a^b L(x,u)du = \frac{1}{\sqrt{C}}[t(a) - t(b)] \qquad (2.14)$$

The remainder of this chapter consists of Table 2-1, as indicated, and concludes the mathematical disgression required for an appreciation of ESF theory. The next two chapters consist of the experimental portion of this work.

Table 2-1: Examples of Convertor Response Functions

STEPPED
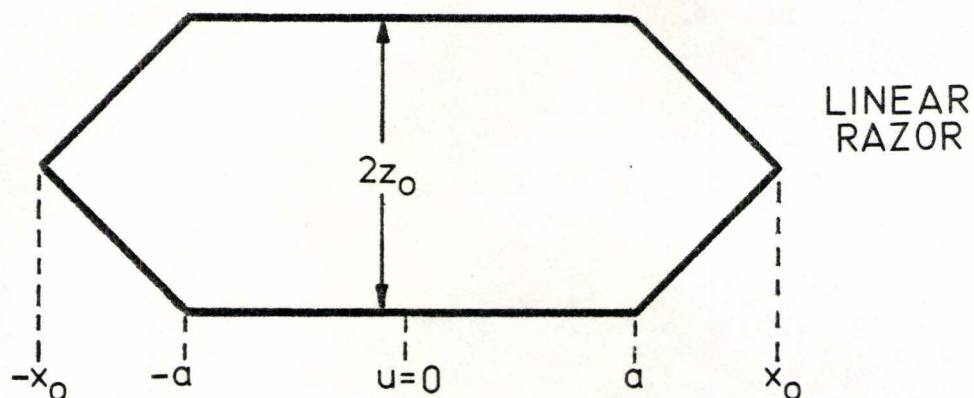BLOCK
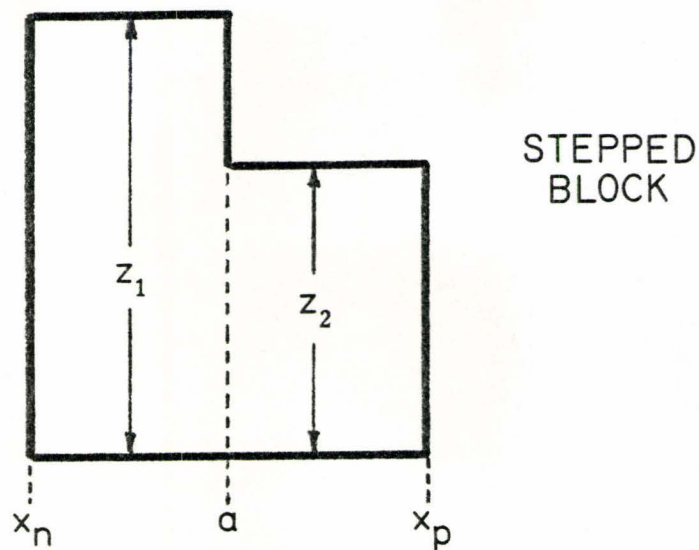
$$\Sigma_a(u,z) = \Sigma, \quad x_n \leq u \leq x_p$$

$$\phi(u) = \begin{cases} e^{-\Sigma z_1}, & x_n \leq u \leq a \\ e^{-\Sigma z_2}, & a \leq u \leq x_p \end{cases}$$

$$P(x) = \frac{\sqrt{c}}{\pi} \int_{x_n}^{x_p} L\phi \, du$$

$$= \frac{1}{\pi} \{ e^{-\Sigma z_1} t(x_n) + (e^{-\Sigma z_2} - e^{-\Sigma z_1}) t(a)$$

$$- e^{-\Sigma z_2} t(x_p) \}$$

Table 2-1 cont'd

LINEAR
RAZOR

$$\Sigma_a(u,z) = \Sigma, \quad 0 \leq |u| \leq x_o$$

$$\phi(u) = \begin{cases} e^{-2\Sigma z_0}, \ 0 \leq |u| \leq a \\ \\ \exp[- 2\Sigma z_0 \cdot \dfrac{(|u| - x_o)}{a - x_o}], \ a \leq |u| \leq x_o \end{cases}$$

$$P(x) = \frac{1}{\pi} \{ \sqrt{c} \int_{-x_o}^{-a} L\phi du + e^{-2\Sigma z_0}[t(-a) - t(a)]$$

$$+ \sqrt{c} \int_{a}^{x_o} L\phi du \}$$

Table 2-1 cont'd

HOLLOW CYLINDER
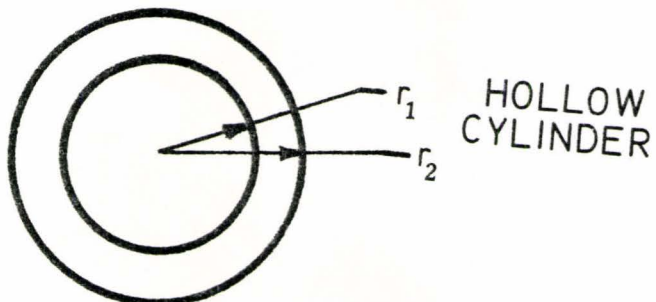
$$\Sigma_a(u,z) = \begin{cases} 0, & 0 \le |r| \le r_1 \\ \Sigma, & r \le |r| \le r_2 \end{cases}$$

$$\phi_1(u) \equiv \exp\left[-2\Sigma \sqrt{r_1^2 - u^2}\right]$$

$$\phi_2(u) \equiv \exp\left[-2\Sigma \sqrt{r_2^2 - u^2}\right]$$

$$P(x) = \frac{\sqrt{c}}{\pi}\left\{ \int_{-r_2}^{-r_1} L\phi_2 du + \int_{-r_1}^{r_1} L\phi_1\phi_2 du + \int_{r_1}^{r_2} L\phi_2 du \right\}$$

3. SIMPLE EXAMPLES OF THE APPLICATION OF ESF METHODS

In this chapter, the theoretical functions derived for the geometries men-
tioned in Section 2.2 will be compared to the densitometer scans obtained
from experimental radiographs; in this manner, the usefulness of the ESF
methods in predicting optical density patterns will be illustrated. In
addition, some of the drawbacks of the method will be examined. Specifically,
problems with the Lorentzian coefficient and with the converter response/
optical density transformation will be discussed.

One of the sources of experimental error here arises from the choice
of materials used in the models. In constructing the various objects, comp-
romises had to be made between low scatter-to-absorption ratios, and availa-
bility and ease of handling. Thus, one settles for aluminum models instead
of silver or gold.

The particular geometries chosen for examination were the stepped
block, the linear razor and the hollow cylinder (see the figures in Table 2-1);
the results are shown in figures 3-1a, 3-1b and 3-1c, and include
the different results for linear and quadratic fits of convertor response to
optical density. The results are good, considering the crudity of the
measurements. In particular, dimensional calibration causes some problems,
since corrections are required for beam divergence (which causes image magni-
fication) and for beam intensity variations (the non-uniform profile creates
some uncertainty in exactly how one should scale the data). The former is
of little importance, since it can be approximately corrected for by use of
the beam collimation ratio; however, the beam intensity profile cannot
properly be accounted for without the considerable computational work required
for a de-convolution procedure. Thus, some judgement is required in
associating density variations with specific object features.
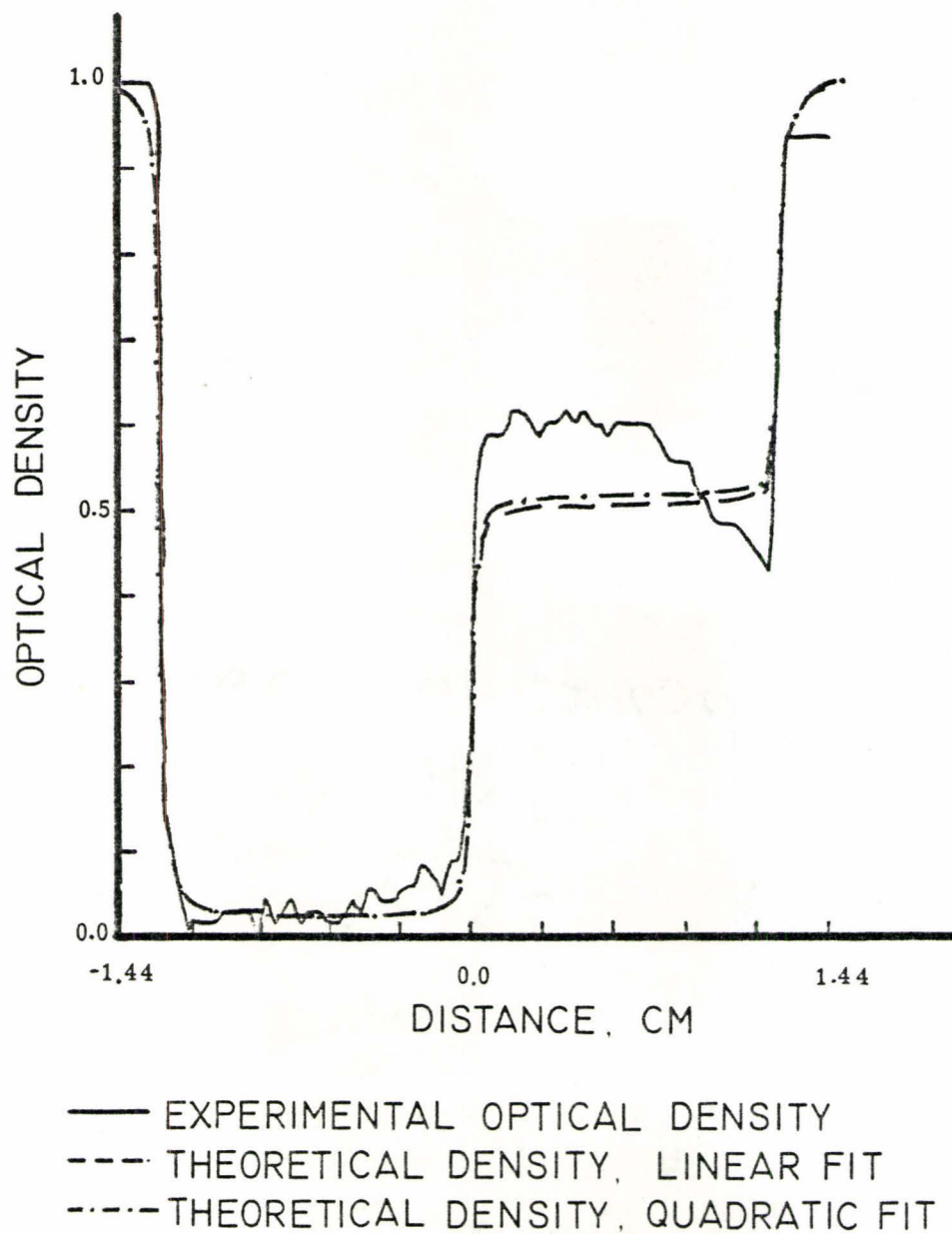
Fig. 3-1a: Theoretical and experimental optical density curves for a stepped block. Note the effects of beam asymetry in the right-hand portion of the curve.

Fig. 3-1b: Theoretical and experimental optical density curves for a linear razor. Only the right half of the curve is shown. Note the apparent negative densities, due to film and densitometer noise.

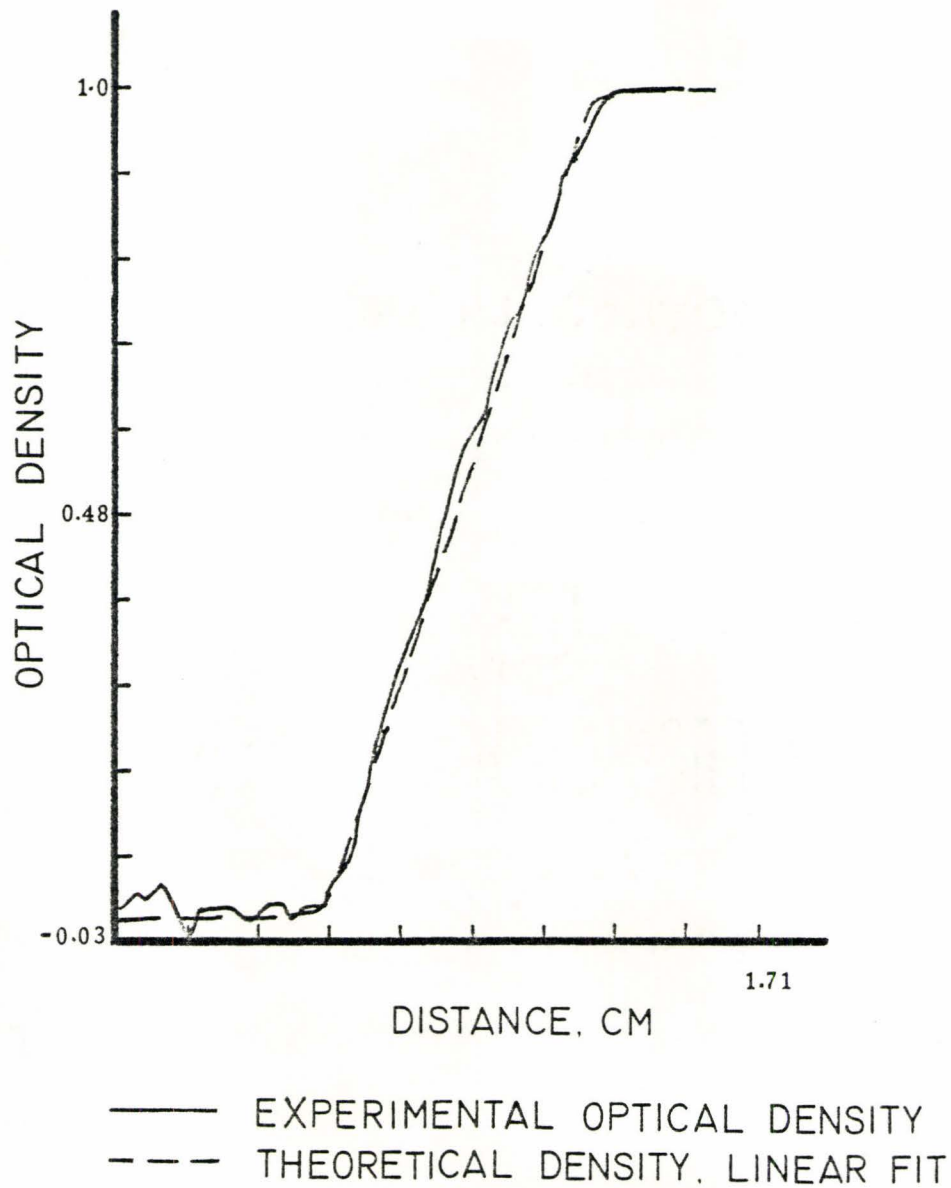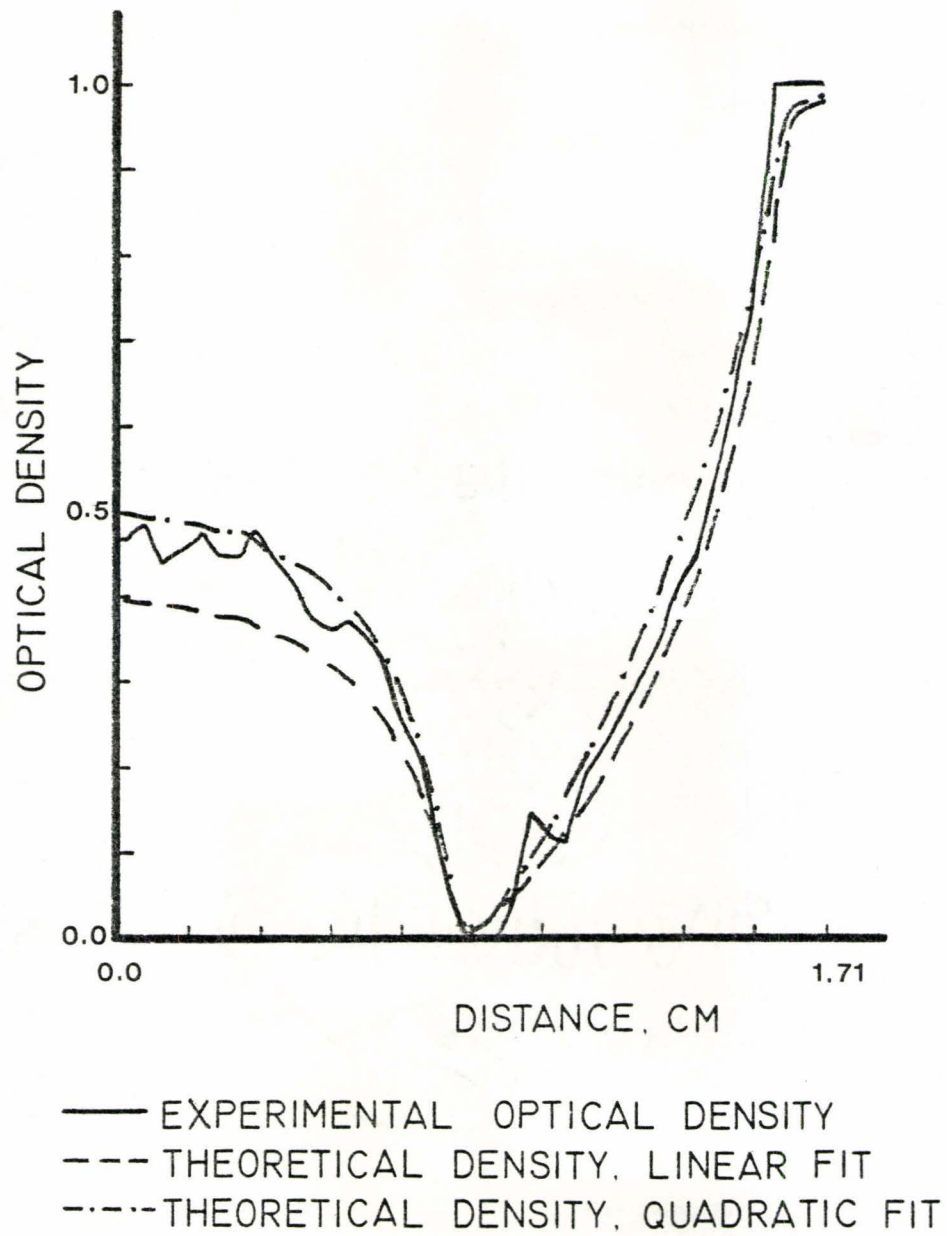Fig. 3-1c: Theoretical and experimental optical density curves for a hollow cylinder. Only the right half of the curve is shown.

The effects of the beam variations are particularly evident in figure 3-1a, which shows the results for the stepped block. The roughness of the right-hand portion of the curve makes it impossible to scale the data exactly; however, in the other regions of the curve, the fit of the theory to the experiment is quite good, particularly the horizontal scaling. Notice that the beam asymmetry is only a serious problem with the larger objects; the range of interest in figure 3-1a is about 2.5 cm (1.0 in.), while in figures 3-1b **and** 3-1c the range is about 1.3 cm (0.5 in.), and thus there are fewer obvious major deviations in the experimental curves. Note that only the larger variations are due to the beam profile; the smaller and more numerous "blips" are due to a combination of chart-recorder machine noise, and finite film grain size. This is particularly apparent in figure 3-1b, where the "noisiness" in the bottom portion of the curve meant an average value had to be used as a base value of the density; thus, negative values were obtained.

The next point of interest is the matter of the convertor response-to-film density transformation. From the figures, it is apparent that the choice of a linear or quadratic transform, i.e.

$$D = a_0 + a_1 S_A$$
$$D = b_0 + b_1 S_A + b_2 S_A^2$$

$$(3.1)$$

is not a major factor, at least for the range of optical densities considered here. Figure 3-1a shows very little difference between the transformations, and in figure 3-1b there was so little difference that the quadratic form is not shown at all.

The reason for considering the second-order transform at all is more or less entirely past experience. Previous work[4] has shown that the quadratic can provide a better fit, and this is verified by examination of figure 3-1; overall, the quadratic transformation fits the experimental curve much better than does the linear fit.

The geometries considered here illustrate the difficulties of using a quadratic or higher polynomial transform; for example, with the stepped block there are three distinct regions of constant optical density (not considering beam asymmetry), and thus three coordinate pairs $(S_A^{(i)}, D^{(i)})$ ($i = 1,2,3$) can be found, so that the second-order transform can be calculated with little difficulty.

When the hollow cylinder is considered, finding the points is slightly more difficult; two points, corresponding to the centre of the scan and the region where the density tends to unity, can be determined quite easily. However, the third point will have considerably more uncertainty associated with it, for two reasons: first, the variation of optical density over small distances is greater, hence the finite size of the densitometer search head means one is using an average value, $\bar{D}$, rather than a discrete value, $D^{(i)}$. Secondly, assigning a specific spatial location to a value is easy. for $S_A^{(i)}$, since it is a calculated value; however, it is not usually a simple matter for $D^{(i)}$, because of the averaging referred to previously and occasionally because of the nature of the equipment used (i.e. hand-held spot densitometers versus scanning micro-densitometers).

Finally, the same problems exist for the linear razor as for the hollow cylinder, only to a greater extent, at least for this case: the variation of density with x is even greater than for the hollow cylinder, and thus the uncertainties in the values of the third coordinate pair become very

significant. This may be the reason why the linear and quadratic fits were so similar in this case.

Clearly, there is room for considerable error in this aspect of the ESF techniques. However, the problems can be minimized by use of better equipment (specifically, densitometers with some form of distance calibration), and, if need be, working with high optical densities, where a linear transformation will be quite sufficient.

Examination of figures 3-1a, 3-1b, and 3-1c shows that the fit of the theory to the experimental curves differs primarily at or about the edges of the objects: the experimental curves are somewhat better defined. Initially, this was thought to be due to numerical round-off error in the computer program written for this purpose, since the majority of the cases involved a numerical integration of the equation for the convertor response. However, this idea was discarded when it became apparent that the edge-smoothing effect was almost as bad for the cases where an exact solution of the integral could be obtained. Additionally, the library integration routine used in the program has been tested enough to guarantee a high degree of accuracy in the results. Thus, the error due to numerical round-off or truncation is acknowledged, but is dismissed as being insignificant.

Another possible cause of the error is the ever troublesome Lorentzian coefficient. This parameter determines (or, more accurately, is related to) the half-width of the Lorentzian spread function, and thus it determines the amount of "smoothing" which occurs about an object edge or other discontinuity. This effect is illustrated in figure 3-2, which shows the value of the convertor response at the edge of a linear razor as a function of C_L. By definition of the range of the convertor response, the values which are greater than unity do not make physical sense, since they imply that one is getting more radiation
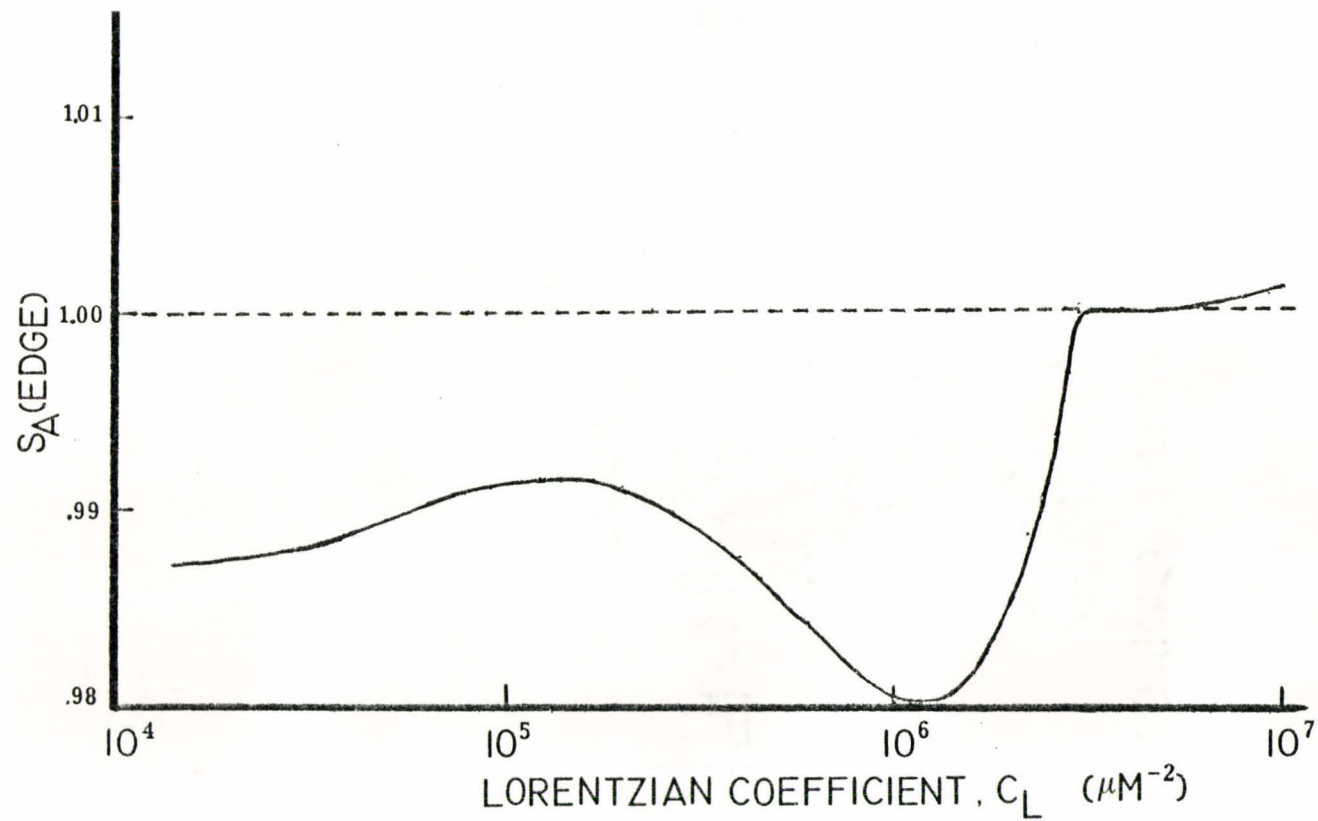
Fig. 3-2: The value of the convertor response at the edge of a linear razor, as a function of the Lorentzian coefficient.

out of the convertor than went in. However, not all of the less-than-unity values are acceptable either; the computer results showed that, for C_L greater than the value which gives a minimum S_A (edge), greater-than-unity values of S_A are obtained, which do not fit into the theory, as stated previously. The reason for this may be that as one lets C_L tend to infinity, the Lorentzian becomes a delta-function in the limit; however, computers do not handle limiting processes very well in some cases, and thus the results obtained may be of a rather dubious nature. Hence, it is suggested that this effect may be considered as a sort of "alarm system" for the validity of the Lorentzian coefficient used. Notwithstanding, one should realize that this is only a suggested explanation, and thus should be considered with caution.

A more plausible cause of the edge smoothing effect is the following: the radiographic facility used for this work is a vertical through-tube set up as described in the previous chapter. Unfortunately, the design of the VTT is such that the radiation beam is not solely composed of thermal neutrons; the actual composition is approximately 70% thermal, 25% γ-rays and 5% epithermal neutrons. The epithermals are of no concern, since they interact inefficiently with both the x-ray film and the gadolinium converter foil. However, the γ-ray portion of the beam is of considerable interest to this work, since γ-rays interact quite efficiently with film. As a result, one need not consider any spreading effects (since there is no secondary radiation involved in the image formation), so that the optical density due to γ-radiation will be proportional to the attenuated γ-flux, and the convertor response:

$$D(x) = N_\gamma \phi_\gamma(x) + N_n \int_{u=-\infty}^{\infty} L(x,u)\phi_n(u)du \tag{3.2}$$

where ϕ_n and ϕ_γ are the attenuation functions for neutrons and γ-rays respectively, and N_γ and N_n are normalization factors. This is not meant to be a definitive representation of the dual-process density function, of course; the true form is likely to be much more complicated. The point to be made is that this representation of $D(x)$ will reflect the discontinuities which may occur in ϕ_γ and ϕ_n, but which are masked in ϕ_n by the spreading of the secondary radiation; thus, this form for $D(x)$ will be much "sharper" or more nearly discontinuous at the object edges. However the dual-process density is formulated, it is a systematic error which cannot be removed without extensive re-design of the existing experimental set-up. Contrarily, the theoretical model can be adjusted to compensate for the presence of different radiations.

One very simple method of examining this problem is to assume that the total optical density is equal to a sum of optical densities caused by specific radiations; in this case, one obtains

$$D_{total} = D_\gamma + D_n \tag{3.3}$$

where D_γ is the density for the indicated radiation. Now, assume that the density due to a particular kind of radiation is proportional to the amount of radiation in the beam; thus, correcting for the epithermal portion of the neutrons,

$$\frac{D_\gamma}{D_{total}} = \frac{.30}{.90} \tag{3.4}$$

This approach may not be strictly correct, since it assumes that interactions with the film emulsion are similar for both the beam γ-rays and the convertor secondary radiation. This may not be the case, since the beam γ-radiation is likely to be of higher energy than the thermal neutrons and can potentially cause multiple reactions in the emulsion. Neglecting this, substitution of the previous result into equation (3.3) gives

$$
\begin{aligned}
D_n &\approx D_T \left[1 - \frac{0.3}{0.9}\right] \\
&= \frac{2}{3} D_T
\end{aligned}
$$

(3.4)

If this result is compared to the theoretical results, some improvement may be obtained. However, this idea will not be pursued further, since the approach described here is terribly over-simplified, and the results would not be particularly significant. The presence of other radiation than thermal neutrons should be noted, and considered in the examination of the results.

This concludes the discussion of the elementary applications of ESF methods. As has been indicated, there is considerable room for improvement in the technique, but the areas of uncertainty are such that they can be optimized or, in some cases, eliminated. A particular thorn in the side of this researcher is the Lorentzian coefficient; however, some interesting alternative means of dealing with this parameter have been developed elsewhere[4]. In the meantime, the present chapter should have illustrated the basic uses of the method; in the next chapter, an application to a practical problem will be discussed.

4. THE APPLICATION OF ESF METHODS TO THE MEASUREMENT OF FUEL ELEMENT
   DIMENSIONS

The purpose of this chapter is to illustrate, from a more
realistic point of view, both the virtues and the drawbacks of
ESF methods. This was made possible by what amounts to a stroke of
luck: a model fuel element containing natural and enriched uranium
was made available to various institutions in Canada and the United
States for neutron radiographic studies, and McMaster happened to
be one of the institutions chosen. In particular, this facility
was chosen because "considerable work is being done on the theoreti-
cal solution of the problems connected with dimensional measurements".[8]

When one is involved in the analysis, management, and solution
of the various problems associated with the utilization of fissile
reactor fuels, a means of obtaining useful data is necessary. To
get information from experiments on fresh fuel is relatively straight-
forward, since there is little or no radiation hazard, although there
is the problem of the chemical toxicity of plutonium fuels; however,
once the fuel has been exposed to a reactor environment, handling
it in a manner suitable for the acquisition of numerical data becomes
a rather complicated business. Thus, various indirect techniques of
measurement are necessary.

One of the techniques which has found some application is
neutron radiography; the method is particularly appropriate, since
a fuel element continues to produce neutrons for some time after
removal from a reactor core (although at a greatly reduced rate). The
disadvantages lie in the fact that the fission products which are

generated in the element by the irradiation of the fuel tend to emit various radiations which are quite capable of causing film blackening (i.e. a γ-radiograph) and in addition prevent easy handling of the fuel.

The solution to these problems is to use an alternative method called transfer radiography; this involves exposing a metal foil made of some material with a large absorption cross-section (e.g. dysprosium-164) to the irradiated element, so that the emitted neutrons cause it to become activated. This is done either under water or in a very heavily shielded facility. After a suitable "exposure" time, the foil is placed in contact with a radiographic film, such that the secondary radiation causes an image to form. The result is a "true" neutron radiograph, since the film does not "see" any γ-radiation from the object or in the radiation "beam". With care, the quality of a transfer radiograph can be made comparable to that of a directly-obtained radiograph.

As will become apparent, it was possible to use a direct approach in obtaining the radiographs used in this work; however, it is thought that with some modification of the theory it will become possible to apply the model to transfer radiography. While this work deals only with dimensional measurements of irradiated fuel elements, the advantages of having a method of predicting image patterns for both direct and transfer methods can best be illustrated by

listing some other areas where neutron radiography of irradiated fuel has been proven useful; this is done in Table 4-1. Further details can be found in the references given.

The construction of the element is shown in figure 4-1 and the details of dimension and material are listed in Table 4-2. Not shown in the figure are the zircalloy end-caps on the tube, or the retaining (zircalloy) springs located at both ends, which hold the eight fuel pellets in place. As may be apparent, the pin is designed to permit measurements of the pellet diameters and the width of the gaps between the pellets (fuel) and the zircalloy tube (cladding). It should be pointed out here that the values of the diameters of the ground-down portions of the pellets are based on values supplied by the pins owner, hence the high degree of accuracy.

The absorption cross-sections for the various pins were calculated by assuming that the microscopic cross-section for uranium dioxide was the same as that of uranium. This is justified by noting that the cross-section for oxygen is only about one-twentieth of that of ^{238}U, and is about four orders of magnitude smaller than that of ^{235}U. Note that for uranium or other fissile materials, the capture cross-section must be used in the calculations; that is to say, one must consider absorption and capture-leading-to-fission processes, since both result in the removal of neutrons from the beam. Any

Table 4-1: Areas of Application of Neutron Radiography in Irradiated
            Fuel Element Analysis.

Area of Application	References
Dimensioning various irradiated materials.	9, 10, 11, 12
Measurement of creep and stress.	13
Uniformity of property changes and isotopic distribution.	14
Dimensioning of heat-transfer gaps to determine the location of "hot spots"	15

PIN NO.

8

7

6

5

4

3

2

1

ZIRCALLOY
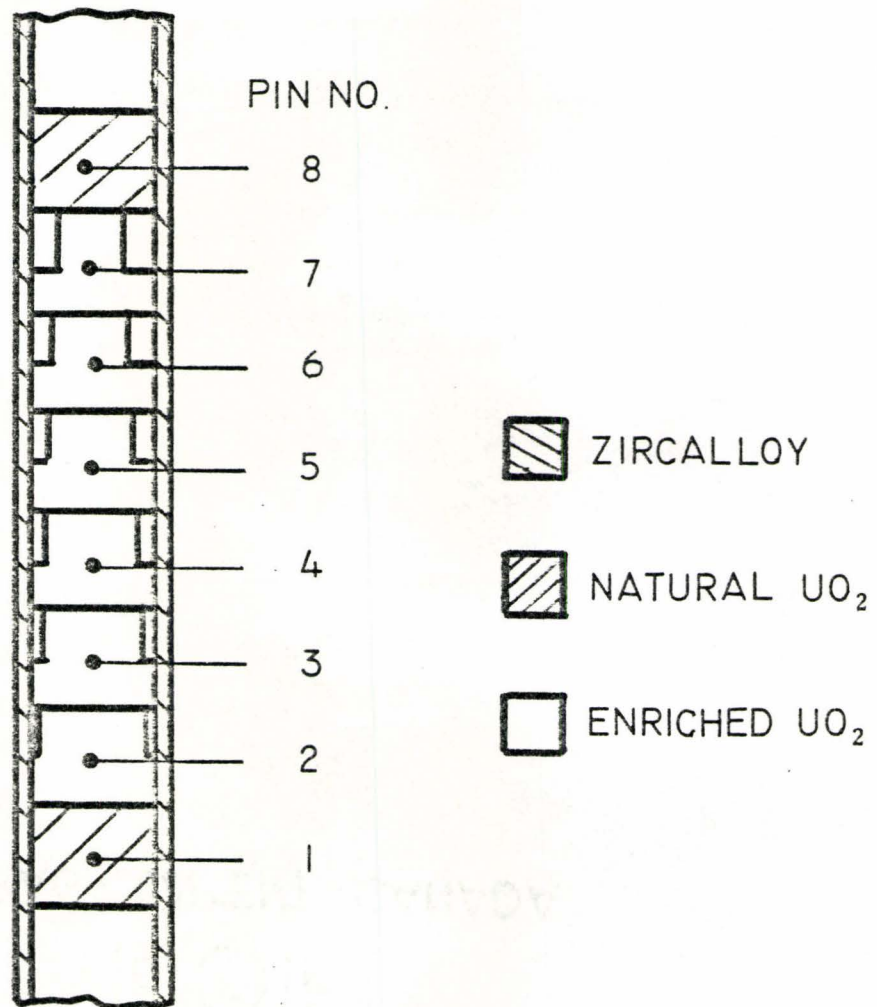
NATURAL UO$_2$

ENRICHED UO$_2$

Fig. 4-1: The construction details of the RISO model fuel element. The end-caps and the retaining springs are not shown.

Table 4-2: Details of the Fuel Elements Construction.

Pin No.	Material	R_1(cm)	Material	R_2(cm)	Material	R_3(cm)
1	Nat. UO_2	.6322	Zircalloy	.715		
2	Enriched UO_2	.627425	Air	.6325	Zircalloy	.715
3	Enriched UO_2	.622426	Air	.6325	Zircalloy	.715
4	Enriched UO_2	.617425	Air	.6325	Zircalloy	.715
5	Enriched UO_2	.611950	Air	.6325	Zircalloy	.715
6	Enriched UO_2	.606425	Air	.6325	Zircalloy	.715
7	Enriched UO_2	.602150	Air	.6325	Zircalloy	.715
8	Nat. UO_2	.6322	Zircalloy	.715		

Material	Absorption cross-section[16] (cm^{-1})
Zircalloy	0.0096 or 0.1453 (see text)
Natural UO_2	0.1831
Enriched UO_2 (3.15%)	0.5918

possible effects of fast neutrons generated in this manner are neglected
since they interact efficiently with neither film nor convertor; further-
more, it is unlikely that they can be moderated down to thermal energies
in the distance between the pin and the convertor. Some problems with
the cross-section for the cladding arose during the analysis; however,
the discussion of this factor will be momentarily postponed.

A brief mention of the experimental details is appropriate here:
the pins were radiographed using Kodak T film with an exposure time of
fifteen minutes. The peak portion of the beam was used for all shots,
and to further ensure consistency in the positioning, a small aluminum
cradle was used. This device was constructed so that the pin was centred
over a slot in the aluminum, with the slot width being somewhat greater
than the outside diameter of the pin. Additionally, the edges of the
slot were coated with a very thin layer of gadolinium oxide paint; this
appeared in the radiographs as a thin white line, and allowed more accur-
ate dimensional scaling. The micro-densitometer magnification was set
to 4X (the lowest possible on this machine), with a scanning field size
of approximately 1.0 mm x 0.1 mm.

The results are shown in graphical form in figures 4-2a through
4-2h; the various figures show the optical density for each pin as a
function of the radial coordinate and the cladding cross-section. The
left- and right-hand sides of the density curves are shown together
for each pin, even though there was enough of an asymmetry effect (due to
the beam intensity profile) to cause minor problems with the vertical
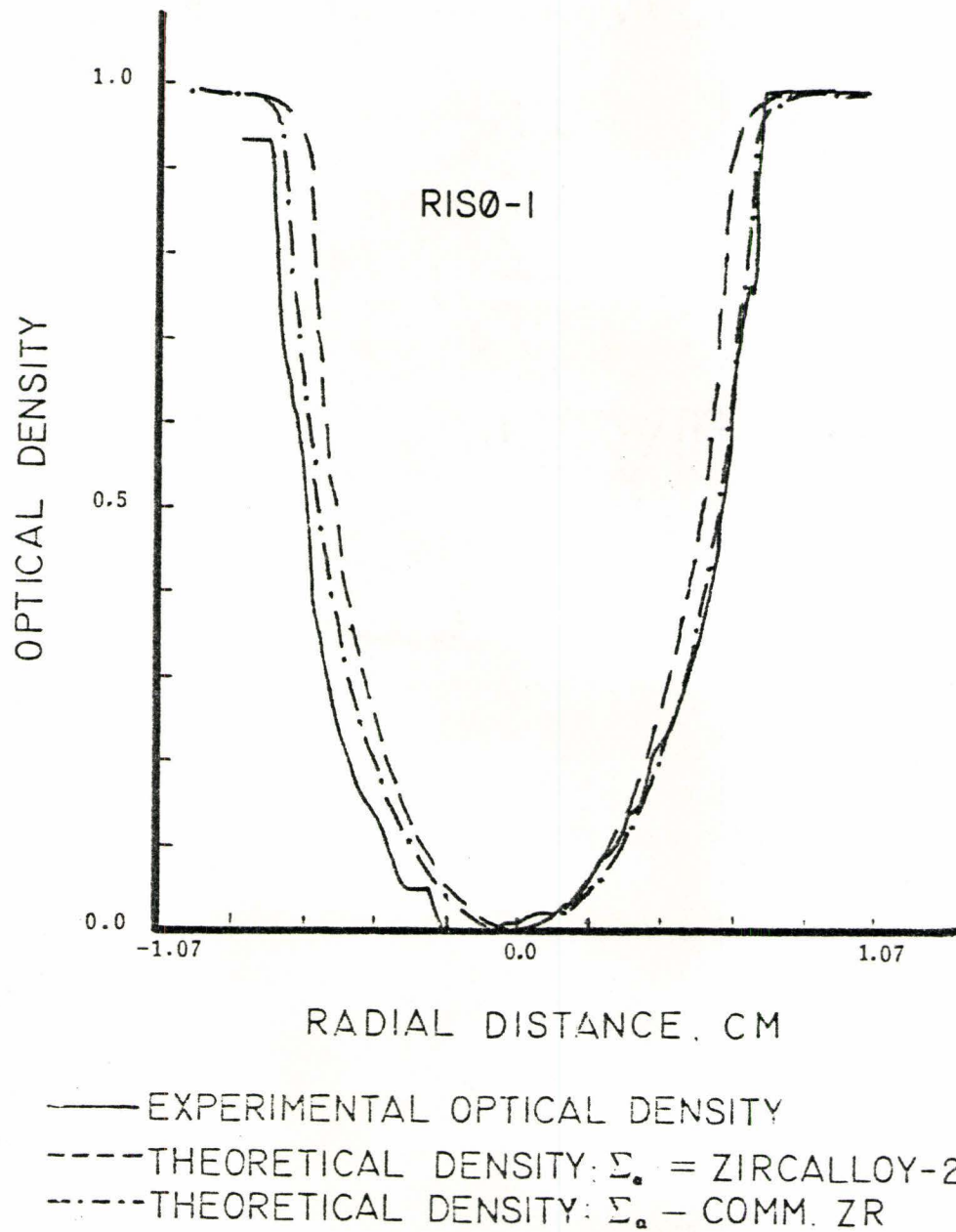scaling. For convenience, all curves have been scaled to the range

Fig. 4-2a: Theoretical and experimental results for the optical density curves for RISØ-1. Note the asymmetry in the left-hand side of the experimental curve which may be due to a defect in this pellet.
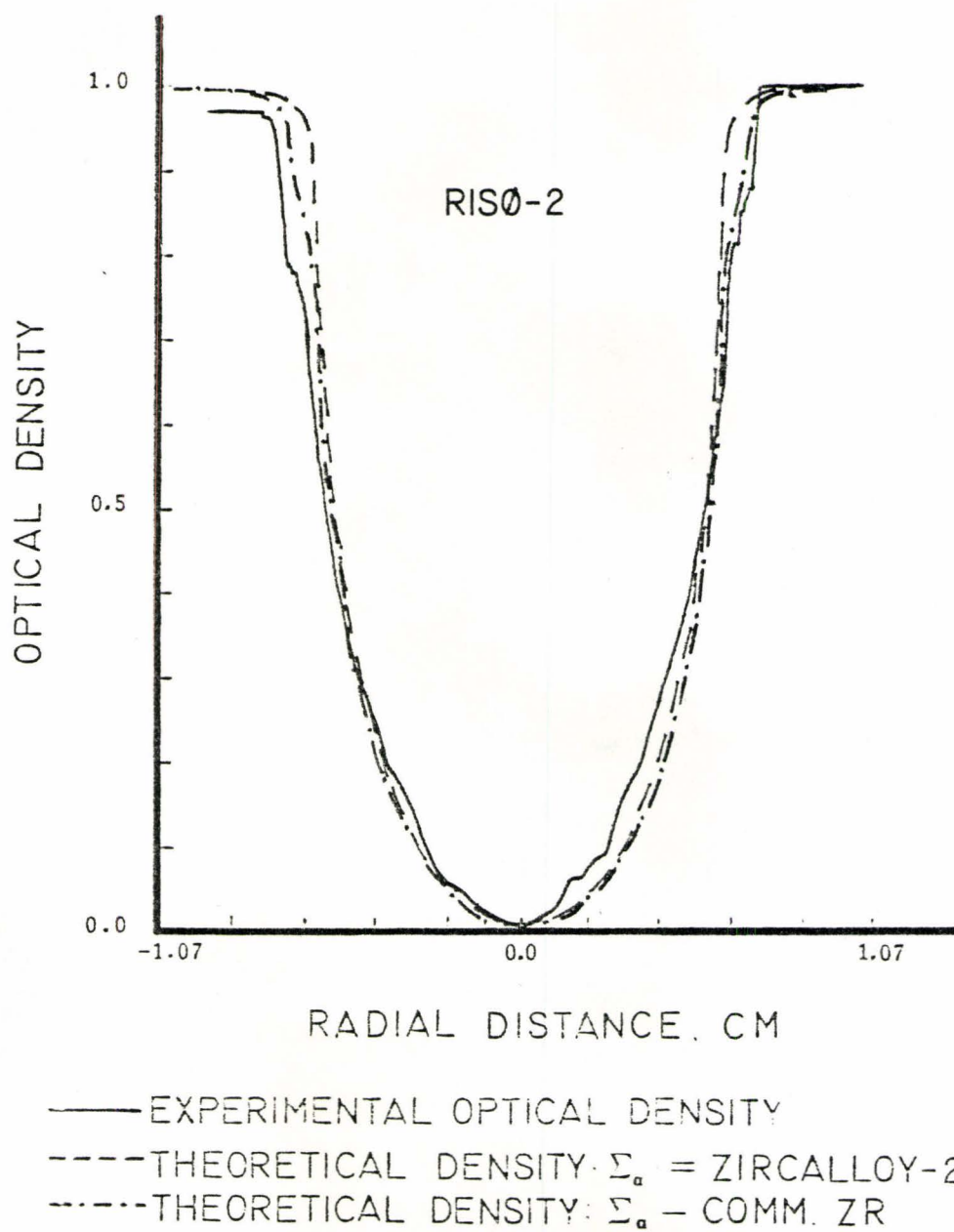
Fig. 4-2b: Theoretical and experimental results for the optical density curves
for RISØ-2.

Fig. 4-2c: Theoretical and experimental results for the optical density curves for RISØ-3.

RISØ-4

OPTICAL DENSITY

1.0

0.5

0.0

-1.07   0.0   1.07

RADIAL DISTANCE, CM

———— EXPERIMENTAL OPTICAL DENSITY

- - - - THEORETICAL DENSITY Σ_c = ZIRCALLOY-2

-·-··THEORETICAL DENSITY Σ_a – COMM. ZR

Fig. 4-2d: Theoretical and experimental results for the optical density curves for RISØ-4.
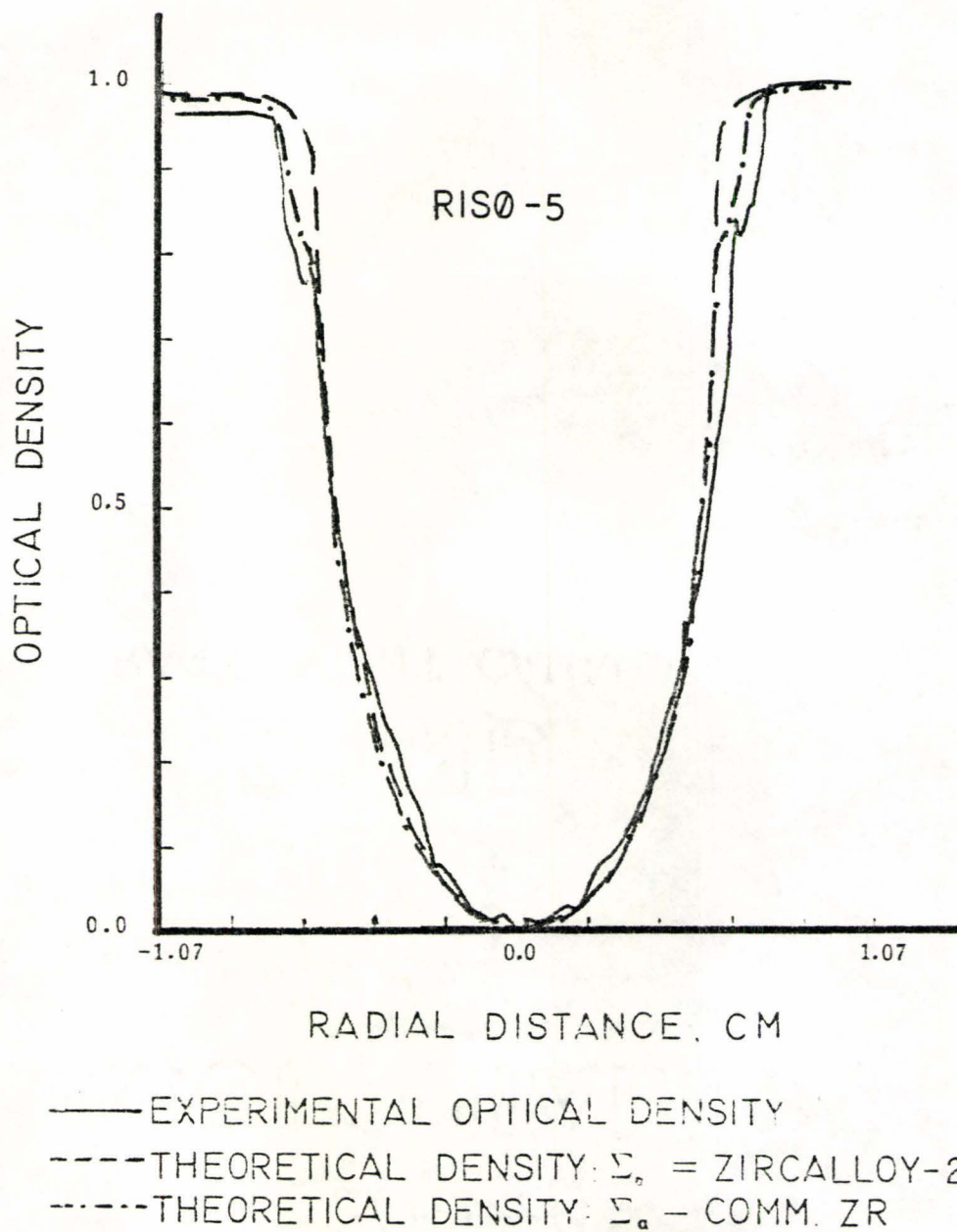
Fig. 4-2e: Theoretical and experimental results for the optical density curves for RISØ-5.

Fig. 4-2f: Theoretical and experimental results for the optical density curves for RISØ-6. Note the asymmetry in the right-hand side of the experimental curve, corresponding to a defect in this pellet.

Fig. 4-2g: Theoretical and experimental results for the optical density curves for RISØ-7. Note the asymmetry in the left-hand side of the experimental curve which may be due to a defect in this pellet.

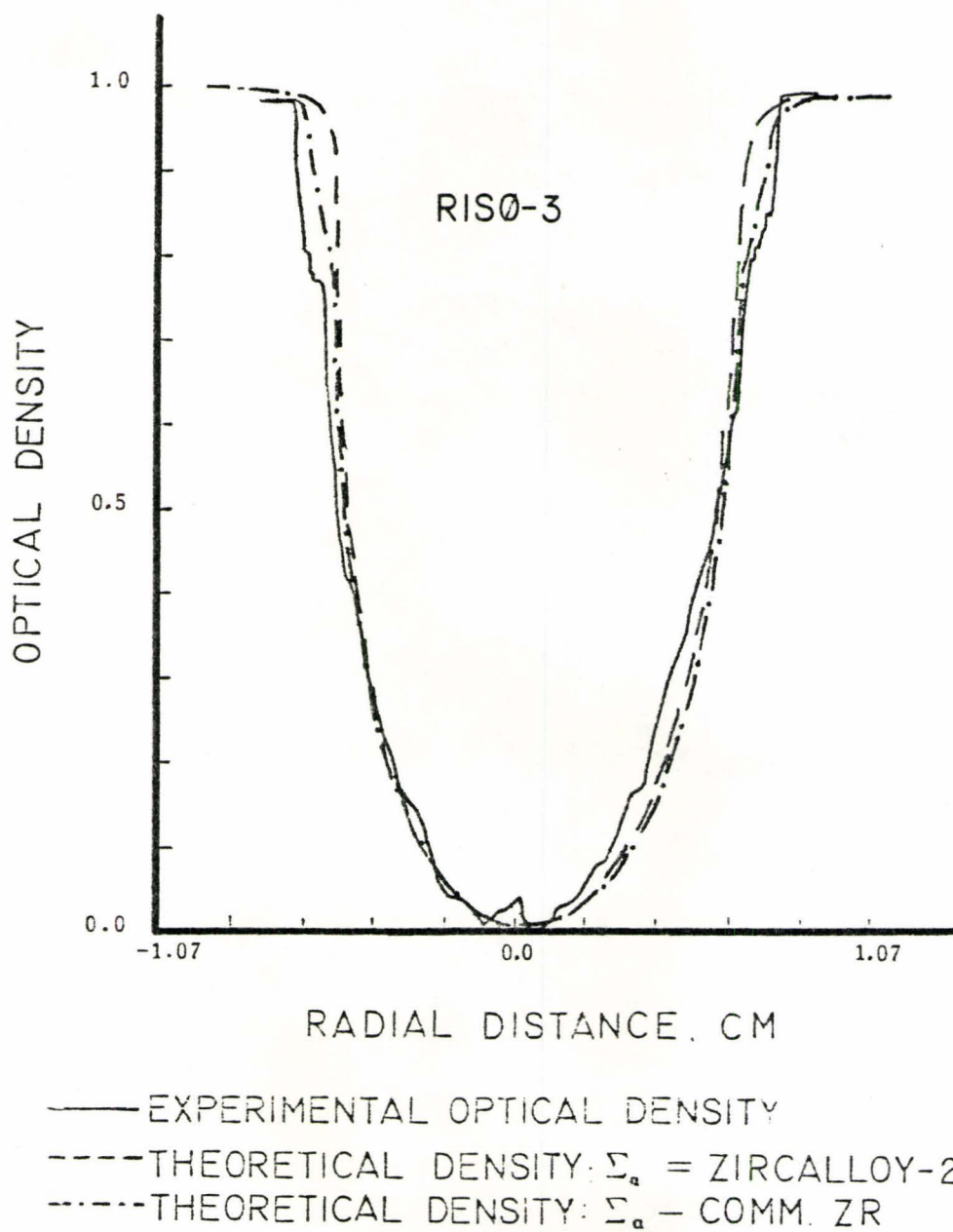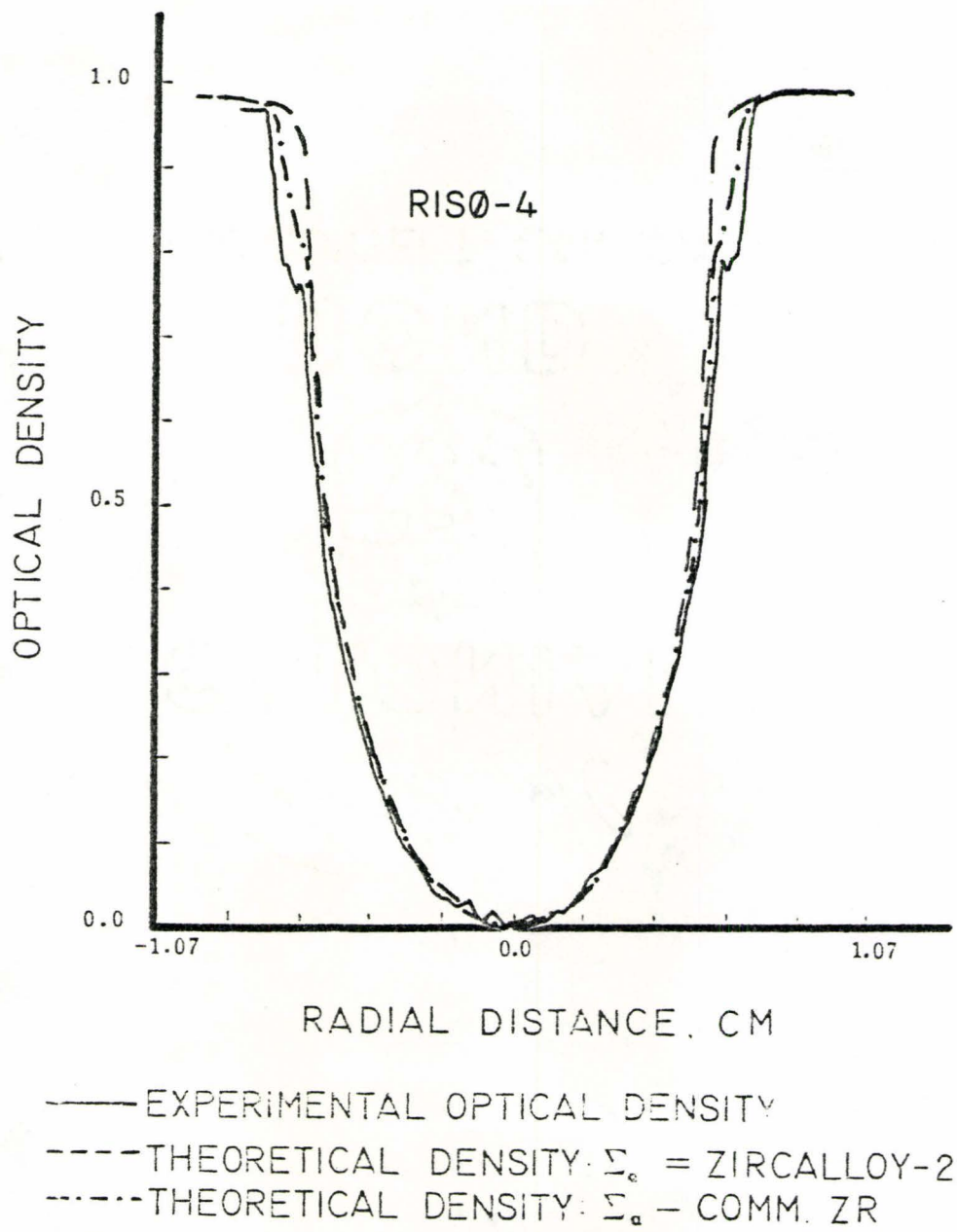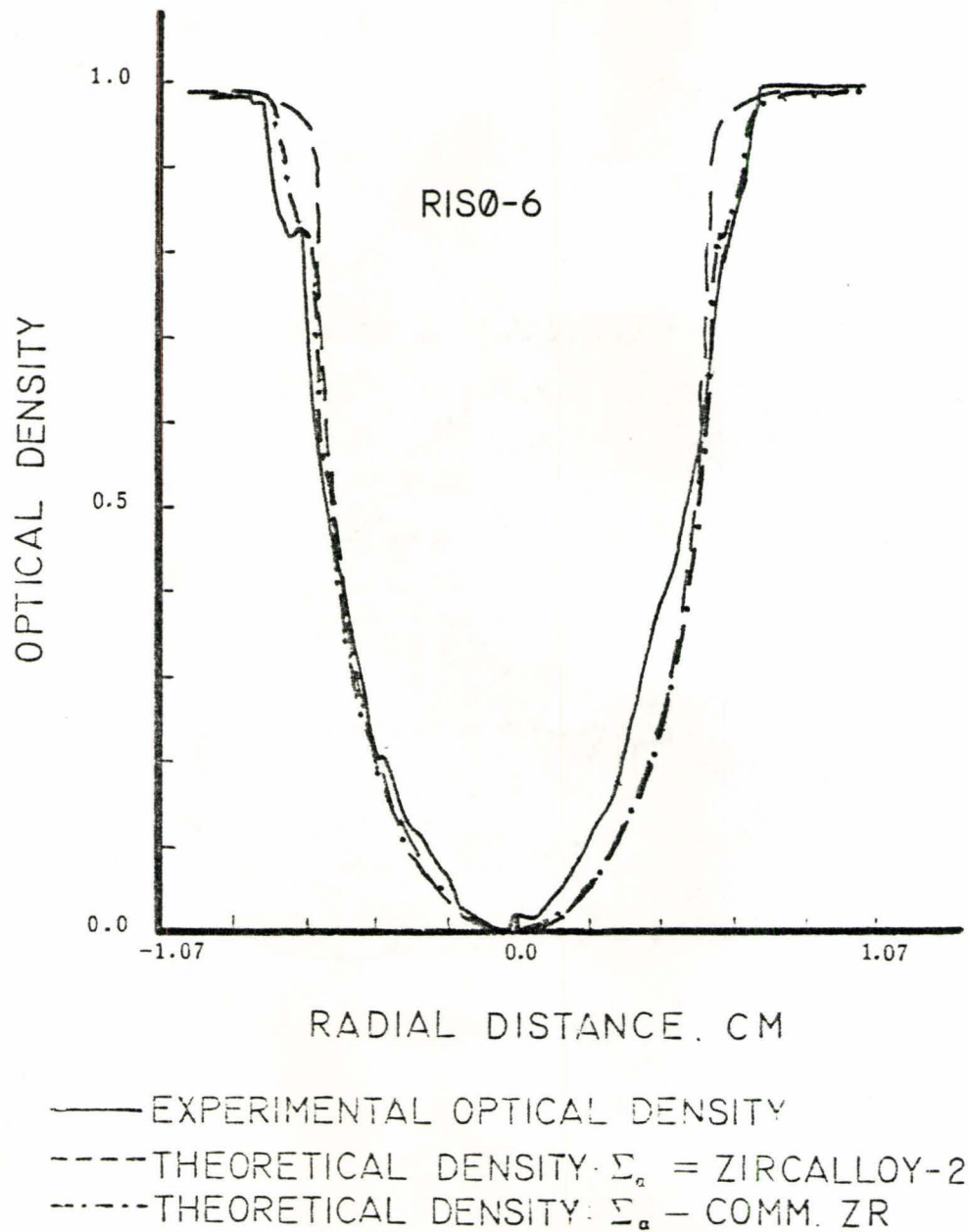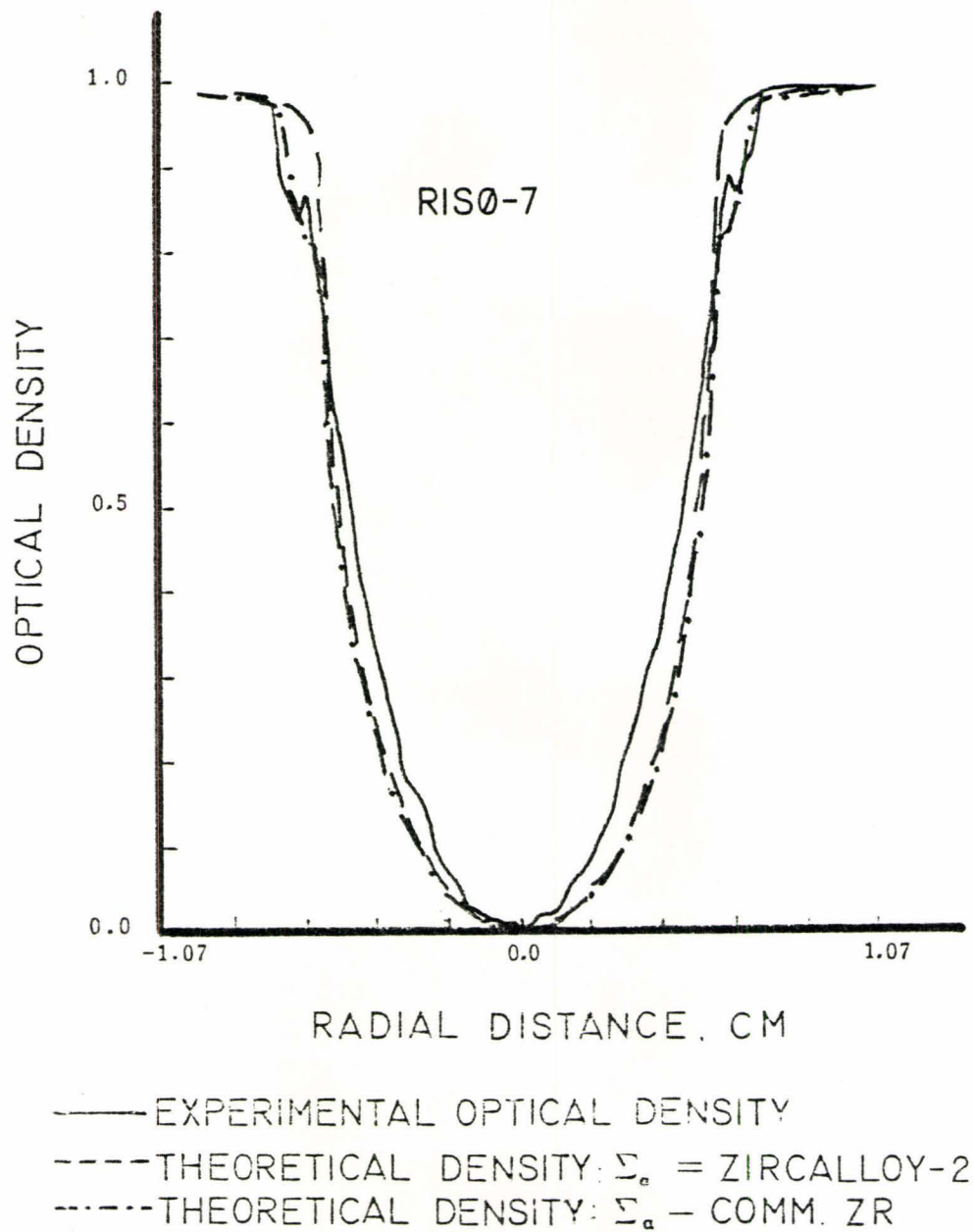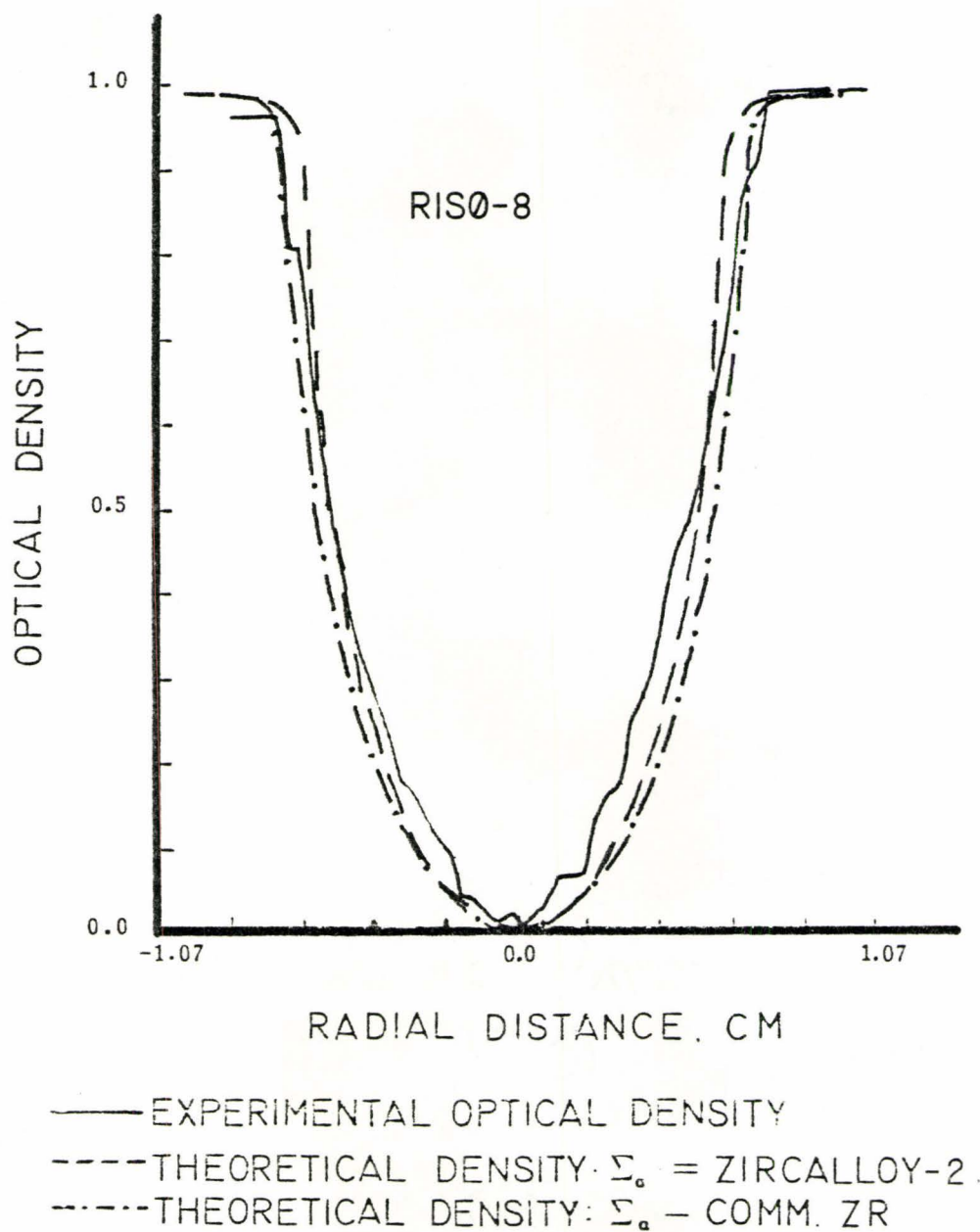Fig. 4-2h: Theoretical and experimental results for the optical density curves for RISØ-8.

(0., 1.0); in passing, it should be noted that the curves followed the expected pattern of larger drops in density (relative to the maximum value) for the enriched fuel than for the natural fuel pellets and a smaller drop in density as the pellet diameter decreased.

Viewed as a whole, the results are excellent, and further indicate the possible usefulness of this method in dimensioning problems; however, when the figures are examined on an individual basis there are a number of points of contention. The most serious of these is the matter of the absorption cross-section for the cladding; this is illustrated in the figures by the sets of dashed lines. The information provided by the owners of the pin stated that the cladding was zircalloy, but it did not specify whether it was zircalloy-2 or zircalloy-4. A visual examination of the radiographs suggested the cladding was made of zircalloy-2, since it is clearly visible in all the shots; this might be due to the presence of nickel in zircalloy-2, which has a fairly high absorption cross-section. At any rate, the "2" form was assumed, and the initial calculations were run on this basis. As is apparent from the figures, the results are dubious: there is no evidence of the gap between the pellet and the sheath for even the largest cases, and there is little or no evidence of the sheath itself. Additionally, in some of the cases, the overall fit of the theoretical curve is, basically, dismal.

Initially, this was thought to be a numerical problem, so the various cases were re-run with an extremely fine calculation mesh. This gave no improvement. Then, some calculational experiments were conducted with the value of the Lorentzian coefficient, on the assumption that perhaps the line-spread function being used was too broad, and thus

could have an overall smoothing effect on the curve. This also was of
no help; in fact, the various curves obtained only helped to illustrate
the problems caused by C_L in the limiting process described in chapter
3.

Finally, the cross-section value for the cladding was changed;
the value used was that of so-called commercial zirconium, which con-
tains various other elements in addition to pure Zr. As can be seen
in the figures, this greatly improved the fit of the theoretical curves
to the data (in most cases); not only is the general fit of the curve
excellent but the object features appear almost exactly as they do on
the experimental curves. The gaps are not as well-defined on the theoretical
curves, but this is thought to be due to a combination of LSF smoothing
effects, uncertainty in the cross-section values, and possibly the pre-
sence of γ-radiation in the beam. As mentioned previously, γ-rays interact
with the film without the aid of a convertor screen, and as a result
object discontinuities may be more accurately reflected in the radio-
graphic image, and thus in the resulting line-scans.

Some of the pins contained various defects, in the form of cracks;
this is clearly visible in figures 4-2f and 4-2g corresponding to pins
number 6 and 7. Each of these had a crack on the right side and as a
result the agreement between theory and experiment is particularly poor
here: no allowance was made for these defects when the attenuation
function, $\phi(u)$, was defined. One cannot properly say whether or not this
effect was a contributing factor to the errors in the other curves, since
the viewing angle specified for the radiographs was fixed; thus, one
cannot determine from a visual inspection whether or not the other pins

might have been cracked. However, because of the obvious difference between theory and experimental data in the cases of known defects, it seems unlikely that the others could contain large cracks.

Of the apparently undamaged pins, the cases of least agreement correspond to the two end pins, which are made of natural uranium dioxide. In particular, for either value of Σ_a(cladding) the sheath does not clearly show up in any of the theoretical curves, whereas in both of the experimental curves there is a region on the curve which can easily be associated with the cladding region. It is not entirely clear why the sheath does not show up well in the curve for the left side of pin number one; it may be due to a defect, or to some temperamental quirk of the micro-densitometer. However, the point of importance is that the sheath is not clearly visible in the theoretical curves. This is a matter of some concern, since the point of having a theoretical model is to be able to predict the effects of such features. The only plausible explanation is that the values of the cross-sections for the two regions are close enough to "smooth out" most of the variation; this can be seen from inspection of the attenuation function for a two region cylinder:

$$- \frac{1}{2} \ln[\phi(u)] = \Sigma_2 [\sqrt{R_2^2 - u^2} - \sqrt{R_1^2 - u^2}] + \Sigma_1 \sqrt{R_1^2 - u^2} \qquad (4.1)$$

R and Σ are the radius and cross-section for the i-th region. Note that this equation only holds for $|u| \leq R_1$. Equation (4.1) can be re-written as

$$- \frac{1}{2} \ln[\phi(u)] = \Sigma_2 \sqrt{R_2^2 - u^2} + (\Sigma_1 - \Sigma_2) \sqrt{R_1^2 - u^2} \qquad (4.2)$$

Clearly, if Σ_2 and Σ_1 are nearly equal, then the attenuation is basically determined by the outer region (Σ_2, R_2); contrarily, if Σ_2 is very small, the atteunation will be determined by the inner region (Σ_1, R_1). This is what has occurred for the natural uranium dioxide pins: for zircalloy-2

the latter result holds, while for commercial zirconium, the former is the case. The point that matters is that the theoretical curve will be approximately equal to that which one would obtain for a single-region cylinder, i.e., the sheath will not be easily visible in the theoretical curve. This is a point which should be kept in mind when using ESF analyses, since this "masking" effect could lead to serious errors; indeed, it is not unlikely that this has happened with the other pins. However, it may be possible, as was done here, to vary the cross-sections in such a manner as to cause object features to be more easily visible. While this will seriously affect the general usefulness of the method in dimensioning problems, it should not prevent the use of ESF techniques in predicting optical density "trends" (i.e. the overall shape of a curve as opposed to the finer details). In passing, it should be noted that for the natural fuel pins, the zircalloy-2 cross-sections provide a better fit to the data, in that there is a small deviation in the theoretical curve corresponding to the location of the cladding. This suggests that the problem with the other pins was due to the relative values of the cross-sections, as previously discussed; inspection of the figures indicates that apart from the matter of the fuel pin gaps, the fit for Σ_a (cladding) = 0.010 cm^{-1} is comparable to that for Σ_a (cladding) = 0.145 cm^{-1}. The only major exceptions are the results for the left-hand sides of pins number 1, 6, and 7; for 6 and 7, this is because of material defects. For number 1, there may be a defect, but this cannot be properly ascertained; hence, this particular result must be regarded with caution.

To close this chapter, a summary of the highlights seems appropriate. First, there are the sources of error; these consist of

noise problems due to film grain and the analyzing equipment; dimensional problems, in scaling the data, because of the non-uniform beam intensity; the presence of γ-radiation, in the beam itself and from the slightly active pins; a very small error due to not-quite-perfect beam collimation; computational errors resulting from numerical integration; uncertainty in the value of the Lorentzian coefficient; and uncertainty concerning the values of absorption (or capture) cross-sections. While this may appear to be a fairly formidable array of errors, it should be pointed out that four of the seven causes of error are negligible, and the remaining three can be discussed and accounted for, at least on a qualitative basis. Another error which has not been mentioned is the matter of neutron scatter; while not a major problem for uranium, object scatter may be significant in other cases. However, the model used here cannot properly account for scatter without extensive modification, so the subject must be passed over with the warning that it could be a serious problem: Σ_s is not always smaller than Σ_a, and this could lead to significant deviations from the absorption-only model, particularly (and unfortunately) near the object edges.

In concluding this chapter, it seems appropriate to point out that while there is a need for improvement and refinement of the present edge-spread function methods (particularly in the extension of the theory to account for object scatter and different types of radiation), there is every indication that the model is already a viable technique worthy of further development.

5. SUMMARY AND CONCLUSIONS

In the preceding chapters, some simple experiments which were intended to test the validity of ESF theory were described, and the various results were presented and discussed. The overall trend of these results was to indicate that the method has the potential for considerable generality and utility, subject to certain qualifying conditions. In order to illustrate this, a summary of the major points will be provided, along with conclusions which may be more obvious when this work is viewed in its entirety.

Chapters 1 and 2 consisted of the necessary background material. Specifically, chapter 1 discussed the physical aspects of image formation, the convertor response-optical density relationship, and the experimental facilities, while chapter 2 considered the mathematics of edge-spread functions and their use in describing neutron radiographic image formation. Here, it was shown that an expression could be derived for the convertor response due to any material/geometry combination with relatively little difficulty; the method of derivation is particularly amenable to computer treatment.

In chapter 3, the basic application of the theory to predicting optical density patterns was considered. A number of simple objects were examined, and in doing so it was shown how the usefulness of ESF theory depends on the ideality of the experiments: when the conditions are greatly different from those implied in the assumptions used to derive the ESF models (cf. chapters 1 and 2), the agreement between the data and the theory begins to break down. In particular, non-uniformity of the incident neutron beam profile and the presence of other radiation than neutrons in the beam may seriously affect the applicability of ESF methods. It would be useful to generalize the ESF model to include those situations where the incident beam is non-uniform (for example, when a divergent collimator is used); however, it is not difficult

to correct the simpler cases on an empirical basis, which may be a simpler approach if one is dealing with routine applications. To correct for the effect of other radiations is a non-trivial matter, since these other radiations tend to interact with the "radiographic system" (the sample and the film) in a more complex fashion; this could be the subject of considerable future investigation. For the present, it can best be dealt with by modifying the experimental facility.

Some difficulties with the numerical aspects of the ESF method were discussed; the various results indicated that the choice of a linear or a quadratic relationship between optical density and convertor response was a rather arbitrary matter, and one might as well use the linear transform to simplify calculations. This would be particularly useful in the average application, where "precision" involves millimetres, rather than micrometres; also, as mentioned, quadratic effects appear to be prominent only in the low optical density region, where very little practical work is done: to obtain useful information from a radiograph, one requires fairly high optical densities (cf. section 1.4).

Some problems with the Lorentzian coefficient were encountered; in particular, it was shown how certain values of C_L lead to non-physical values of convertor response. It is not clear as to whether or not this was only some sort of numerical phenomenon; looking at these and earlier experiments[2,3], it appears that this problem may be connected to the experimental facility. As mentioned, there is some γ-radiation in the beam, and this tends to "sharpen up" the radiographic images (cf. chapter 3). Now, values of C_L are obtained by fitting ESF functions to experimental data; if these data represent neutron and gamma image formation processes, then it is not strictly correct to use the basic ESF functions of chapter 2 unless the γ-rays represent a negligible

fraction of the beam make-up. It is obvious that the resolution of this matter will depend on further investigation.

In chapter 4, a practical problem was considered, with encouraging results. Although the methods of obtaining an image of an irradiated fuel element would be quite different in practice, it was suggested that only slight modifications to the theory would be required to accomodate these "different methods". Overall, the correlation between the experimental data and the predicted results was good; however, under close scrutiny, some further problems were encountered.

When the absorption cross-sections of the various materials in the pin were calculated it was found that there was some doubt as to exactly what the pin was made of. In an assembly line situation, where one is examining some fraction of the total production, this could not occur: material properties would be specified, and one would look for deviations from the norm, particularly with regard to object geometry. That the ESF methods are suitable for this purpose is well illustrated by the cases of cracked fuel pellets, where there was a distinct difference between the theoretical and experimental results, even allowing for cross-section error. This difference would be even more apparent in a production situation, where all parameters are known; here, the uncertainty in cross-section implies further uncertainty in any dimensions obtained through use of ESF techniques, because the functions used to calculate these dimensions also depend on material properties. This was particularly apparent for the fuel pin cladding; it was clearly shown how the mathematics could be given more than one physical interpretation. This implies, naturally enough, that care must be used with ESF methods. It was then suggested that in cases where multiple explanations of the ESF results are possible, it might be more suitable to use the technique to predict trends arising from object property variations, rather than trying to pinpoint details.

The conclusions are the remaining matter of importance, and there appears to be four points of particular significance. First, it would appear that the ESF methods can be successfully applied to "real" problems, as well as to "textbook" cases; that is to say, one can predict with some degree of accuracy the optical density pattern for a fairly complicated combination of geometry and materials, as well as for the very simple cases considered previously. This leads into the next idea, which is that certain combinations of material and geometry may reduce that degree of accuracy to the point where only trends can be predicted, rather than exceedingly fine details; this means that some caution will have to be exercised when applying the method to dimensioning problems. The third point is not entirely resolved, but the basic idea is that if one is only interested in trends (that is, predicting the broad form of an optical density pattern), then it is possible to use artificial values of the cross-sections to "enhance" the appearance of certain object features. This was done here by using the cross-section for a material similar to the one which has apparently been used. It may be possible to do this in such a manner as to facilitate a dimensioning procedure, but this must remain a matter of speculation for the time being. Finally, one should emphasize a point which was made earlier: the ESF method as used here is specifically set up for neutron radiography; however, it appears that the end results may be quite sensitive to other features of the radiographic facility. In particular, if there are other radiations present in the beam (or if the object being radiographed is giving off some form of radiation), then the ESF results may be limited in their accuracy by the extent of the available information concerning the radiation fields present in or around the facility.

It is apparent that the ESF method of neutron radiographic image analysis is a flawed technique; it is strictly applicable to a situation which

may not be easily realized in practice. However, the results of the work
presented here indicate that the method is not without its merits; there is
definitely an excellent case for applying this theory to simple situations, and
this implies that the model will be a good first approximation for more compli-
cated theories. Additionally, for non-destructive examinations where only
moderate accuracy is required, ESF methods should be of great utility. Thus,
it is suggested that the edge-spread function methods of analysis be further
investigated, both for use with other models and for its inherent interest
as a basic investigation tool.

REFERENCES

1. Harms, A.A., Garside, B.K., and Chan, P.S.W., "The Edge-Spread
   Function in Neutron Radiography", J. Appl. Physics, 43, (1972).

2. Butler, M.P., "Studies in Neutron Radiography", undergraduate
   thesis, Dept. of Engineering Physics, McMaster University, Hamilton,
   Canada (1978).

3. Harms, A.A., "Recent Theoretical-Experimental Correlations in
   Neutron Radiographic Imaging", in "Radiography with Neutrons",
   British Nuclear Energy Society, London (1975).

4. Butler, M.P., "Neutron Radiographic Imaging Analysis", Master's Project,
   Dept. of Engineering Physics, McMaster University, Hamilton,
   Canada (1980).

5. Herz, R.H., "The Photographic Action of Ionizing Radiations",
   John Wiley and Sons, Inc., New York, N.Y. (1969).

6. ——————— "Determining Image Quality in Thermal Neutron Radiographic
   Testing"; ASTM E545-75 (1975).

7. Berger, H., "Practical Applications of Neutron Radiography and
   Gaging", ASTM-STP-586 (1976).

8. Domanus, J.C., Private communication.

9. Cutforth, D.C., "Dimensioning Reactor Fuel Specimens from Thermal
   Radiographs", Nucl. Tech., 18 (1967).

10. Robertson, T.J.M., "Neutron Radiography in the Precision Measurement
    of Irradiated Materials", in "Radiography with Neutrons", BNES,
    London, (1975).

11. Domanus, J.C., "Accuracy of Dimension Measurements from Neutron
    Radiographs of Nuclear Fuel Pins", Proceedings, Eighth World Conference
    on Non-Destructive Testing, Cannes, France (1976).

12. Harms, A.A., Heindler, M. and Lowe, D.M., "The Physical Basis for
    Accurate Dimensional Measurements in Neutron Radiography", Mat.
    Eval., 36, 5 (1978).

13. Matfield, R.S., "Irradiation Creep Measurement by Neutron Radiography",
    J. Brit. Nuc. Eng. Soc., 11, (1972).

14. Dahlke, L.W. and Robkin, M., "Development of a Method of Neutron
    Radiography of Mixed Oxide Fuels using Radiographic Analogs", Nuc.
    Tech., 12 (1971).

15. Thaler, L.A., "Measurement of Capsule Heat Transfer Gaps using Neutron Radiography", Mat. Eval., 32, (1974).

16. Cross-section values were taken from "Handbook of Tables for Applied Engineering Science", 2nd Ed., edited by R.E. Bolz and G.L. Tuve; CRC Press, Inc. (1976).